



Time-Resolved Spectroscopy and Electronic Structure of Mono- and Dinuclear Pyridyl-Triazole/DPEPhos-Based Cu(I) Complexes

Merten Grupe^{+, [a]}, Pit Boden^{+, [b]}, Patrick Di Martino-Fumo^{, [b]}, Xin Gui^{, [c]}, Cecilia Bruschi^{, [d]}, Roumany Israil^{, [e]}, Marcel Schmitt^{, [e]}, Martin Nieger^{, [f]}, Markus Gerhards^{, #, [b, g]}, Wim Klopper^{, [c]}, Christoph Riehn^{, [e, g]}, Claudia Bizzarri^{, * [d]} and Rolf Diller^{, * [a]}

This article is dedicated to the memory of our esteemed colleague Markus Gerhards.

Abstract: Chemical and spectroscopic characterization of the mononuclear photosensitizers [(DPEPhos)Cu(I)(MPyrT)]^{0/+} (CuL, CuLH) and their dinuclear analogues (Cu₂L', Cu₂L'H₂), backed by (TD)DFT and high-level GW-Bethe-Salpeter equation calculations, exemplifies the complex influence of charge, nuclearity and structural flexibility on UV-induced photo-physical pathways. Ultrafast transient absorption and step-scan FTIR spectroscopy reveal flattening distortion in the triplet state of CuLH as controlled by charge, which also

appears to have a large impact on the symmetry of the long-lived triplet states in Cu₂L' and Cu₂L'H₂. Time-resolved luminescence spectroscopy (solid state), supported by transient photodissociation spectroscopy (gas phase), confirm a lifetime of some tens of μs for the respective triplet states, as well as the energetics of thermally activated delayed luminescence, both being essential parameters for application of these materials based on earth-abundant copper in photocatalysis and luminescent devices.

Introduction

Coordination complexes employing earth-abundant metals, like copper, have a multitude of applications from solar energy conversion over efficient emitters for new organic light-emitting diode (OLED) materials^[1] to photocatalysis^[2] for small-molecule, for example CO₂, activation.^[3] The increasing demand for

sustainable materials and processes motivates researchers to exploit earth-abundant resources. In particular, coordination metal complexes based on copper in its oxidation state +1 have been addressed as promising alternatives in respect of other complexes based on expensive and rare metals such as ruthenium, iridium or platinum.^[4] Tetracoordinated copper(I) complexes have a pseudo-tetrahedral geometry in the ground

[a] Dr. M. Grupe,⁺ Prof. Dr. R. Diller
Department of Physics
TU Kaiserslautern
Erwin-Schrödinger-Straße 46
67663 Kaiserslautern (Germany)
E-mail: diller@physik.uni-kl.de

[b] P. Boden,⁺ P. Di Martino-Fumo, Prof. Dr. M. Gerhards[#]
Department of Chemistry
TU Kaiserslautern
Erwin-Schrödinger-Straße 52
67663 Kaiserslautern (Germany)

[c] Dr. X. Gui, Prof. Dr. W. Klopper
Institute of Physical Chemistry
Karlsruhe Institute of Technology (KIT)
Fritz-Haber-Weg 2, 76131 Karlsruhe (Germany)

[d] C. Bruschi, Dr. C. Bizzarri
Institute of Organic Chemistry (IOC)
Karlsruhe Institute of Technology (KIT)
Fritz-Haber-Weg 6, 76131 Karlsruhe (Germany)
E-mail: claudia.bizzarri@kit.edu

[e] R. Israil, M. Schmitt, Dr. C. Riehn
Department of Chemistry
TU Kaiserslautern
Erwin-Schrödinger-Straße 52
67663 Kaiserslautern (Germany)

[f] Dr. M. Nieger
Department of Chemistry
University of Helsinki
A.I. Virtasen aukio 1, 00014 Helsinki (Finland)

[g] Prof. Dr. M. Gerhards,[#] Dr. C. Riehn
Research Center OPTIMAS
Erwin-Schrödinger-Straße 46
67663 Kaiserslautern (Germany)

[*] These authors contributed equally to this work.

[#] Deceased December 28th 2020

Supporting information for this article is available on the WWW under <https://doi.org/10.1002/chem.202102760>

 This manuscript is part of a Special Issue "Cooperative effects in hetero-metallic complexes".

 © 2021 The Authors. Chemistry - A European Journal published by Wiley-VCH GmbH. This is an open access article under the terms of the Creative Commons Attribution Non-Commercial NoDerivs License, which permits use and distribution in any medium, provided the original work is properly cited, the use is non-commercial and no modifications or adaptations are made.

state. When excited, the complex populates a metal-to-ligand charge-transfer (MLCT) state since the low-lying metal-centered states are prevented in Cu(I) due to its completely filled d-orbitals (d^{10} metal). In this MLCT state, the copper center is formally oxidized and therefore, the complex undergoes a flattening distortion to arrange in a square planar geometry, which is usual for tetracoordinated Cu(II) complexes. To use Cu(I) complexes as photosensitizers, they should possess a good chemical stability in solution, and an excited state lifetime in the microsecond scale. In order to have an emissive and long-lived excited state, the strategy is to reduce this flattening distortion to a minimum level, which can be afforded by using rigid ligands with bulky substituents. This is the reason why heteroleptic Cu(I) complexes of type (NN)Cu(PP) are gaining attention, as reviewed recently.^[5] Here, (PP) is a chelating diphosphine, such as (9,9-dimethyl-9H-xanthene-4,5-diyl)bis(diphenylphosphane) (Xantphos) or bis(2-(diphenylphosphanyl)phenyl)ether (DPEPhos), and (NN) is the diimine ligand, where usually the LUMO of the complex is localized. In particular, the diimine ligand is often based on 1,10-phenanthroline and derivatives and, with the right substituents, the excited state lifetimes of heteroleptic Cu(I) complexes of this structure can reach up to 20 μ s.^[4a,6] Heteroleptic Cu(I) complexes with pyridyl-triazole as diimine are less investigated. However, they do not only show long-lived excited state lifetimes, but they are usually highly stable in solution, without forming the homoleptic Cu(NN)₂ complex upon time, as it is often the case with 1,10-phenanthroline derivatives.^[7] Since they often present efficient solid-state emission in the light-blue/cyan region, Cu(I) complexes with pyridyl-triazole (or tetrazole) ligands find usually applications in OLEDs,^[8] while their usage as photosensitizers or photoredox catalysts is rather limited,^[3h,9] in contrast to the cuprous complexes based on 1,10-phenanthroline.^[2a,b,10]

Key to the understanding of the related photochemistry is to find correlations between molecular structure and optical properties, i.e. establish a structure-function relationship.^[5] Therefore, the determination of important experimental and theoretical spectroscopic and structural data is central to investigation of such photoactive compounds and fuels the discussion of their application by delivering, for example absorption spectra and assignment of transitions and electronic states, lifetimes of electronically excited states, for example luminescent triplet states, and non-radiative relaxation pathways, quantum yields (if possible), (photo-)stability and reactivity in different environments. It should be emphasized, that the exploration of (ultrafast) time scales and the connections or sequences of elementary photochemical pathways after excitation are essential for gaining fundamental insights into their "functionality" and in parallel supports the rational design of such metal complexes, displaying a highly active field of research.

Specific to Cu(I) complexes is the question of the occurrence and ultrafast time scale of structural relaxation (Jahn-Teller flattening distortion (FD)) in the excited state.^[8b,11] Since FD, within its own temporal evolution, is likely to change rates for internal conversion (IC) and intramolecular vibrational relaxation (IVR), it poses a challenge for the disentanglement of

photoinduced primary processes. This concerns in particular excited electronic state deactivation and lifetime shortening, as well as its involvement in the formation of a long-lived electronically excited state via intersystem crossing (ISC).^[12] The related putative involvement of several low-lying singlet and triplet states has been discussed recently.^[13] Here we report a study on a series of heteroleptic Cu(I) complexes, based on chelating diimine unit 6'-methyl-pyrid-2'-yl-1*H*-1,2,3-triazole (MPyrT), i.e. the two mononuclear complexes [(DPEPhos)Cu(I)(MPyrT)]^{0/+} (neutral **CuL** and cationic **CuLH**), and the two dinuclear complexes, where the diimine units are linked together by a phenyl ring (MPyrT)₂Ph, i.e. [(DPEPhos)₂Cu(I)₂(MPyrT)₂Ph]^{0/2+} (neutral **Cu₂L'** and dicationic **Cu₂L'H₂**). For the reported mass spectrometric and gas phase investigations within this text we abbreviate the cationic complexes explicitly with their charge. These complexes are designed as photosensitizers, envisaging their use in the photoactivated CO₂ reduction in combination with an appropriate (earth-abundant metal-based) catalyst.^[14] We reveal here the new structures of the compounds **CuL** and **Cu₂L'** as received by X-ray diffraction analysis. The molecular structures of all complexes, here under investigation, are based on the same and formative heteroleptic unit **CuL**, and thus allow the comparative study of their chemical and in particular their photophysical properties with regard to charge and nuclearity. To this end we have applied a broad variety of experimental and theoretical methods. Our study also focuses on cooperative effects^[15] apparent as non-additive contributions of dimerization and/or protonation. Most photophysical and electrochemical properties observed, for example for the dinuclear charged system cannot be derived from the characteristics of the protonated monomer and the neutral dimer, which is discussed qualitatively as a kind of cooperative effect. Furthermore, a quantification of cooperativity is presented for the luminescence energies.

Electrochemical analysis and Stern-Volmer quenching experiments were performed to obtain redox and photocatalytic properties, respectively, in particular for the new (neutral) complexes **CuL** and **Cu₂L'**. Time-resolved spectroscopic methods were used to explore photoinduced dynamics. (i) Femtosecond UV/Vis transient absorption (fs-TA) reveals ultrafast processes, such as Franck-Condon-state relaxation, FD and intersystem crossing. Both solution and solid phase (neat film) preparations were addressed to study, in general, the influence of the environment and in particular exploit the extent of environment rigidity on the photodynamics. (ii) Step-scan FTIR spectroscopy was applied to KBr pellets for structural characterization of long-lived excited (triplet) states, the lifetimes of which were determined as function of temperature via (iii) time-correlated single photon counting (TCSPC). The latter yields valuable information on the S₁-T₁ energy gap, crucial for the luminescence efficiency, determined by thermally activated delayed fluorescence (TADF)^[1d,16] via reverse intersystem crossing (RISC). As photophysical properties are prone to matrix effects, (iv) femtosecond and, as a novel variant, microsecond transient photodissociation (τ -PD) in gas phase were applied, allowing direct comparison with the condensed phase measurements. Our experimental results are compared with the results

of high-level quantum chemical computations on the electronic absorption spectra in gas and condensed phase, the IR-vibrational spectra of the long-lived excited triplet states, and the magnitude of FD.

Results and Discussion

Synthesis and structural properties

The heteroleptic copper complexes investigated in this paper were prepared using a commercially available chelating phosphine, the so-called DPEPhos (from bis[(2-diphenylphosphino)phenyl] ether), and diimine ligands based on 6'-methylpyridyl-1*H*-1,2,3-triazole (MPyrT). Pyridyl-triazoles are well known chelating ligands for a variety of coordination metal complexes,^[17] as well for Cu(I), as it is demonstrated by various publications.^[8c,14, 18] As stated in the introduction, despite their high stability in solution, heteroleptic Cu(I) complexes based on pyridyl-triazole have been less investigated. Moreover, beyond the increased stability, our motivation is enforced by the straightforward preparation of such ligands. In this work we followed the two-steps synthesis reported by Bizzarri et al.,^[14] consisting of a Sonogashira cross-coupling reaction between one or two equivalents (for the dichelating diimine) of 2-bromo-6-methyl-pyridine and one equivalent of phenylacetylene or 1,4-diethynylbenzene, respectively, followed by a Huisgen cycloaddition with an excess of NaN₃ at high temperature. The charged Cu(I) complexes **CuLH** and **Cu₂L'H₂** were prepared in dichloromethane (DCM) at room temperature under argon (Ar) atmosphere, by dissolving DPEPhos and Cu(NCCH₃)₄BF₄ together with the corresponding ligand. The neutral complexes **CuL** and **Cu₂L'** were obtained via deprotonation by washing the DCM solution of the respective charged complexes with a saturated aqueous solution of K₂CO₃. In Figure 1, next to the chemical structures of the four complexes, the crystal of the charged dinuclear Cu(I) complex is shown.

Suitable crystals for X-ray diffractometry were obtained only for the charged species, by slow evaporation of solvent (CDCl₃). The colorless crystals of **Cu₂L'H₂** have a monoclinic system with a C2/c space group, whilst the mononuclear **CuLH** crystals are tetragonal with P4₃2₁2 space group, as reported earlier.^[14] In both cases, the geometry around the Cu(I) nuclei is pseudotetrahedral. While the N–Cu–N angles are very similar in the mononuclear and in the dinuclear complexes, (circa 79.9° for both), the P–Cu–P angles are smaller in **Cu₂L'H₂** (111.2° compared to 114.6° for **CuLH**). Dihedral angles between the N–Cu–N plane and the P–Cu–P plane are 92.8° for **CuLH** and 91.3° for **Cu₂L'H₂**. Those values are similar to those calculated for the S₀ ground state (see below). Selected bond lengths and angles are reported in Table SI–1. The complete crystallographic set can be found in the Crystallographic Cambridge Database Center.

Mass spectrometric analysis and fragmentation of ionic complexes

The ionic complexes **CuLH** and **Cu₂L'H₂** were analyzed by electrospray ionization mass spectrometry (ESI-MS) from different solvents (DCM, acetonitrile, methanol) and isolated in an ion trap for interrogation by collision-induced (CID) and UV laser photodissociation (UV PD).

The mononuclear compound [**CuLH**](BF₄) is detected from a methanolic solution as intact molecular ion: [**CuLH**]⁺ at *m/z* 836 (nominal mass). The dinuclear compound [**Cu₂L'H₂**](BF₄)₂, however, is observed as the *deprotonated* monocationic species [**Cu₂L'H**]⁺ at *m/z* 1595 and upon ESI from the precursor [**Cu₂L'H₂**](PF₆)₂ observed both as a [**Cu₂L'H**]⁺ and the counter ion complex [**Cu₂L'H₂**]²⁺(PF₆)[−] (*m/z* 1741). Identification of all species was achieved by comparison of the according isotope patterns (see Figure SI-9). CID and UV PD of [**CuLH**]⁺ both lead mainly to the loss of the neutral ligand LH, so that [Cu-(DPEPhos)]⁺ (*m/z* 601) is detected as ionic fragment. UV PD of

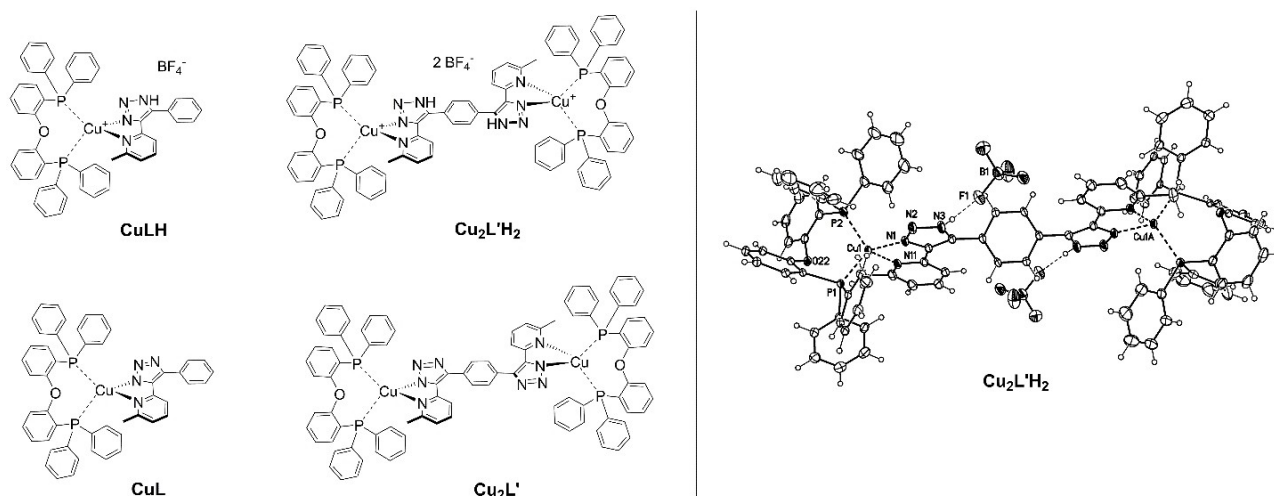


Figure 1. Chemical structures of the Cu(I) complexes investigated in this work (left). Molecular structure of **Cu₂L'H₂** (right).

$[\text{Cu}_2\text{L}'\text{H}]^+$ leads mainly to the loss of N_2 , while CID favours the cleavage of DPEPhos, giving the fragment $[\text{Cu}(\text{L}'\text{H})\text{Cu}(\text{DPEPhos})]^+$ (m/z 1057), and to a lower amount again to the formation of $[\text{Cu}(\text{DPEPhos})]^+$. UV PD and CID of $[\text{Cu}_2\text{L}'\text{H}_2]^{2+}(\text{PF}_6)^-$ results in $[\text{Cu}_2\text{L}'\text{H}]^+$ as the main fragment, whereas the cleavage of $[\text{Cu}(\text{DPEPhos})]^+$ and of LH is also observed. UV PD of $[\text{Cu}_2\text{L}'\text{H}_2]^{2+}(\text{PF}_6)^-$ leads additionally to the loss of N_2 and DPEPhos. In summary, the compound cations have been identified mass spectrometrically and their ion trap isolation proved possible which is a prerequisite for further gas phase laser spectroscopy (see below). CuLH gave intense molecular signals, whereas $[\text{Cu}_2\text{L}'\text{H}_2]^{2+}$ deprotonates easily to form the probably quite stable $[\text{Cu}_2\text{L}'\text{H}]^+$. Overall, the dissociation pathways following thermal (CID) or photoexcitation (UV PD) are similar and limited in variety.

Electrochemical properties and Stern-Volmer quenching

The redox properties of the mononuclear and dinuclear complexes were investigated by cyclic voltammetry (CV) in acetonitrile for the charged species^[14] and in *N,N*-dimethylformamide for the neutral compounds. Tetrabutylammonium hexafluorophosphate (TBAPF_6) was used in all cases as supporting electrolyte. The redox potentials are reported versus ferrocene oxidation, as recommended by IUPAC^[19] and the voltammograms are shown in the Supporting Information (see Figure SI-76). In oxidation, we can identify a one-electron process assigned to the oxidation of the copper metal $\text{Cu}(\text{I})/\text{Cu}(\text{II})$. This process is irreversible for all four complexes. Moreover, there is a light difference when comparing the oxidation potentials of the charged with the neutral species, taking into account that slight discrepancies might also be due to the different solvent used. In particular the neutral compounds CuL and $\text{Cu}_2\text{L}'$ oxidize almost 1000 mV earlier than the corresponding charged species (see Table 1). This is in agreement with the fact that in the neutral species CuL and $\text{Cu}_2\text{L}'$, the $\text{Cu}(\text{I})$ nuclei are coordinated by a negatively-charged diimine, which can stabilize the oxidized form of copper more than the neutral ligand in complexes CuLH and $\text{Cu}_2\text{L}'\text{H}_2$. In the reduction, one irreversible process is present for all complexes around -2.6 V for the neutral species and -2.7 V for the charged complexes. This redox process is localized on the diimine ligand and the 100 mV difference has to be ascribed to the diverse influence of the solvent used. As the first oxidation can be associated to the HOMO level in solution of the corresponding sample, the redox

process correlates well with the theoretical calculation, as it is mainly localized on the metal core $\text{Cu}(\text{I})$. On the other side, the reduction processes are associated to the LUMO levels, and the localization on the diimine is also in agreement with quantum chemical calculation (see below). These assignments are confirmed also by the emission profiles of the four complexes. In fact, the observed emission is broad and unstructured, which is typical for metal-to-ligand charge transfer states.

As we have previously shown for the charged complexes,^[14] the investigated $\text{Cu}(\text{I})$ complexes undergo an oxidative quenching with a nickel(II) 1,4,8,11-tetraazacyclotetradecane (cyclam) complex: $\text{Ni}(\text{cyclam})\text{Cl}_2$, known to reduce CO_2 to CO .^[20] This is demonstrated by Stern-Volmer analysis, which was done in air-equilibrated solutions of the Cu complexes by addition of known aliquots of the nickel(II) complex (Figure SI-75). According to the Stern-Volmer equation, we can extract the apparent quenching constant k_q from the Stern-Volmer constant K_{SV} (see Table 1). The quenching rate is diffusion limited for each $\text{Cu}(\text{I})$ complex, having a k_q of the order of magnitude of $10^{10} \text{ s}^{-1} \text{ M}^{-1}$. When comparing the values between the mononuclear complexes CuLH and CuL , the quenching is twice faster for the protonated compound. This is true also if we compare the quenching rate of the charged mononuclear and dinuclear complexes (CuLH and $\text{Cu}_2\text{L}'\text{H}_2$). Nevertheless, we observe almost no difference between the quenching rates of the charged and neutral dinuclear complexes, as well as the neutral mononuclear and dinuclear complexes. With this, we have demonstrated how these $\text{Cu}(\text{I})$ complexes undergo an oxidative quenching and can potentially act as photosensitizers. Nevertheless, a photoactivated catalysis for CO_2 reduction involves many components and the reaction parameters have to be chosen accurately. Thus, although preliminary photocatalytic tests were done, their results are still not satisfying. Optimizations of the conditions are ongoing and are out of the target of the present work.

Quantum chemical calculations

Quantum chemical computations were performed in order to serve three purposes. Firstly, we have simulated the ground state absorption (GSA) spectra of CuL , CuLH , $\text{Cu}_2\text{L}'$, and $\text{Cu}_2\text{L}'\text{H}_2$ in order to compare these with the experimental GSA spectra measured in CH_2Cl_2 , measured as neat film, and as obtained from gas phase UV laser photodissociation action spectroscopy. Secondly, we have determined the equilibrium structures of the long-lived excited triplet states of CuL , CuLH , $\text{Cu}_2\text{L}'$, and $\text{Cu}_2\text{L}'\text{H}_2$ in order to compare the corresponding computed excited state harmonic vibrational frequencies with the experimental structural characterization by step-scan FTIR spectroscopy (in KBr pellets). Thirdly, we have optimized the equilibrium structures of low-lying singlet and triplet excited states of the mononuclear complexes in order to obtain insight into the flattening distortion (FD) that may occur in the excited states.^[8b,11,21]

We have performed quantum chemical computations at the density functional theory (DFT) and time-dependent DFT (TDDFT) levels using the functionals B3LYP^[22] and PBE0^[23] in

Table 1. Electrochemical potentials of the ground and excited state vs. Fc/Fc^+ and quenching constants.^[a]

Sample	E_{ox}/V	E_{red}/V	$K_{\text{SV}}^{[\text{c}]} / \text{M}^{-1}$	$k_q^{[\text{d}]} / \text{s}^{-1} \text{M}^{-1}$
CuLH	1.30	-2.65	1900	$3.5 \cdot 10^{10}$
$\text{Cu}_2\text{L}'\text{H}_2$	1.93	-2.65	3270	$1.7 \cdot 10^{10}$
CuL	0.49 ^[b]	-2.54 ^[b]	630	$1.5 \cdot 10^{10}$
$\text{Cu}_2\text{L}'$	0.37 ^[b]	-2.56 ^[b]	1190	$1.4 \cdot 10^{10}$

[a] In acetonitrile (0.1 M TBAPF_6). [b] In *N,N*-dimethylformamide (0.1 M TBAPF_6). [c] K_{SV} is the slope of the linear fit $I_0/I = 1 + [Q]$. [d] $k_q = K_{\text{SV}}/\tau$.

Kaiserslautern and in Karlsruhe, respectively. Using these two functionals, the TDDFT optimized equilibrium structures of the low-lying singlet and triplet excited states of the mononuclear systems (**CuL** and **CuLH**) mutually agree very well, giving confidence to having found meaningful structures. States of ligand-centered $\pi\pi^*$ and MLCT character are found as a function of the geometry, making these computations very challenging for TDDFT. For the dinuclear systems, the structural flexibility is even more difficult to handle at the TDDFT level because of the possible mutual orientations of the two fragments and the occurrence of localized (on one fragment) and delocalized (on both fragments) excited states. Therefore, for the systems **Cu₂L'** and **Cu₂L'H₂**, we focus in the following on the geometry optimization of the first triplet excited states and the computation of their harmonic vibrational frequencies at the level of *spin-unrestricted DFT theory* (UDFT). We suspect that the dinuclear systems can be excited locally at both mononuclear fragments of the dinuclear complex, leading to two nearly degenerate localized excited states and an asymmetric complex. Alternatively, two delocalized states (symmetric and antisymmetric) may be found. Not surprisingly, the coordination of the Cu ion in the locally excited state of the dinuclear complex was found to be very similar to the coordination of the Cu ion in the mononuclear complex.

For the computation of the GSA spectra, we have employed the *GW/Bethe-Salpeter equation* (*GW/BSE*) approach.^[24] We have chosen the *GW/BSE* method because we expected to be dealing with charge-transfer states and since TDDFT is known to fail for long-range charge-transfer excited states.^[25] The *GW/BSE* calculations were based on ground-state DFT calculations with the PBE0 functional,^[23] which is common in *GW/BSE* computations.^[24b,c]

For the computation of the equilibrium structures and harmonic vibrational frequencies of the first excited triplet states of the four systems, we have optimized the Kohn-Sham determinant in terms of a UDFT calculation with two unpaired electrons (spin quantum number $M_S = 1$). Since this is a ground-state type optimization, charge-transfer issues are much less severe than at the TDDFT level. Here, we employed the B3LYP-D3(BJ) level of DFT,^[22,26] as done already with great success in many of our earlier works. See, for example Goswami et al. and references therein.^[27]

We have optimized the geometries of the S_0 , S_1 , and T_1 states of **CuL** and **CuLH** at the TDDFT and UDFT (for T_1) levels using the functionals PBE0 and B3LYP. The results obtained with these two functionals mutually agree very well and so do the TDDFT and UDFT results for the T_1 states. The main finding is that FD is observed for all of the excited states except for the T_1 state of **CuL**. For the latter state, the dihedral angle between the P–Cu–P and N–Cu–N planes is nearly 90° , whereas this angle is reduced by ca. 10° in the other three excited states (S_1 and T_1 of **CuLH** and S_1 of **CuL**). We furthermore note that the metal-to-ligand charge-transfer (MLCT) character is significant for the S_1 and T_1 excited states of **CuLH** and for the S_1 state of **CuL**, whereas it is basically absent in the T_1 state of **CuL**. A natural population analysis of the hole and particle unrelaxed difference densities of the T_1 state of **CuL** (in its own T_1 -

optimized geometry) shows that the 3d orbitals of Cu contribute only 1–3% to the unrelaxed hole density (values highlighted with red color in Tables SI-12–SI-14). This contribution is significantly larger (10–40%) for the states that show FD.

Static absorption in condensed and gas phase

The static electronic ground state absorption (GSA) spectra (Figure 2) of the four complexes in DCM as well as neat film are quite similar (besides different overall extinction coefficients), with increasing absorption only below 400 nm. **CuLH** and **Cu₂L'H₂** in DCM show a pronounced shoulder around 350 nm, assigned to a MLCT transition from the Cu atom to the MPyT-respectively the (MPyT)₂Ph-ligand.^[14] This shoulder is not as good observable in the neutral systems, possibly due to stronger overlap with ligand-centered (LC) $\pi\pi^*$ transitions below 350 nm^[14] and less pronounced MLCT character (see Comparison of condensed phase absorption spectra with the theoretical prediction).

In gas phase, i.e. in a room temperature ion trap, we have recorded UV PD action spectra of the ionic complexes which should represent UV absorption spectra (Figures 3, SI-23 and SI-26).^[28] The species **[CuLH]⁺** (Figure 3, blue trace) shows two bands at 270 nm and 305 nm and a less intense feature at ca. 350 nm. The UV PD spectrum of **[Cu₂L'H]⁺** also reveals two bands (270 nm, 315 nm; Figure 3, green trace), however with reversed intensities and a broad shoulder (centered at ca. 330 nm) on the long wavelength side extending up to 400 nm. Additionally, a weak feature could be located at ca. 370 nm. The UV PD spectrum of **[Cu₂L'H₂]²⁺(PF₆)⁻** (Figure 3, red trace) is similar to the one of **[Cu₂L'H]⁺**. However, the broad shoulder at 330 nm is no longer observed, but a weaker band plateau at ca. 350 nm. The absorption spectrum of **[CuLH](BF₄)** (Figures 2 and 3) in DCM overlaps well with the gas phase spectrum, but exhibits less pronounced structures. Instead, it shows a plateau-like shoulder at 290 nm and a shoulder at 350–370 nm. In solution (MeOH, DCM) the spectra of the dinuclear **[Cu₂L'H₂](BF₄)₂** and **[Cu₂L'H₂](PF₆)₂** complexes are both red-

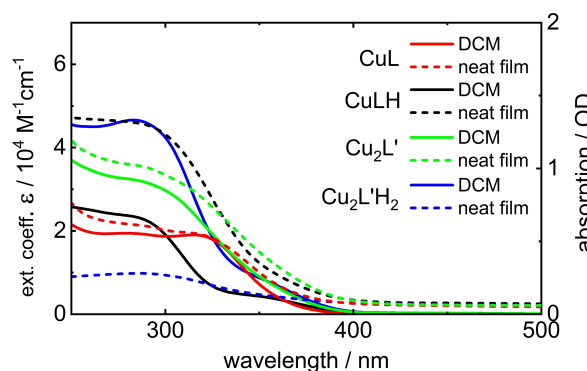


Figure 2. Static UV/Vis absorption spectra of **CuL**, **CuLH**, **Cu₂L'** and **Cu₂L'H₂** in DCM (solid) as decadic ext.-coeff. (solvent contributions subtracted), and as transparent neat film (dotted) in OD units (offset above 400 nm due to scattering), at room temperature. Excitation for UV/Vis fs-TA at 350 nm.

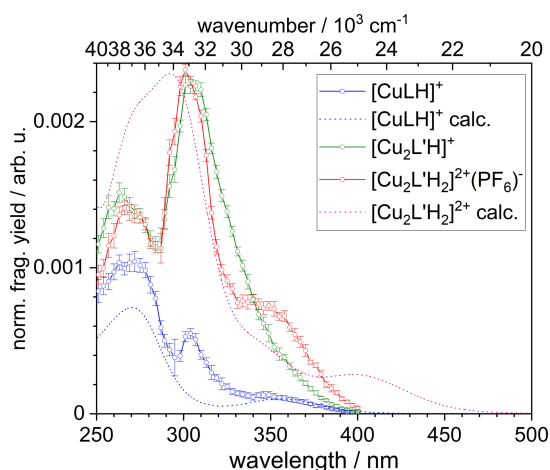


Figure 3. UV PD spectra of $[\text{CuLH}]^+$, $[\text{Cu}_2\text{L}'\text{H}]^+$ and $[\text{Cu}_2\text{L}'\text{H}_2]^{2+}(\text{PF}_6)^-$ and the calculated absorption spectra of $[\text{CuLH}]^+$ and $[\text{Cu}_2\text{L}'\text{H}_2]^{2+}$ obtained at PBE0/evGW-BSE/def2-TZVP level and convoluted with 1500 cm^{-1} full width at half maximum (FWHM).

shifted with respect to the spectra of the mononuclear ones (Figure SI-24). They display a similar behavior with more distinct band structure in gas phase (Figure SI-25). In addition, the absorption spectra obtained in methanol reveal a slight blue-shift by ca. 15 nm with respect to DCM (Figure SI-24), but nearly no change in spectral shape.

In summary, the gas phase spectra exhibit two pronounced band structures in the region of the plateau feature found in solution. The solution spectra are slightly red-shifted with respect to the gas phase spectra which we ascribe to stabilization by solvation, however the onsets on the red side of all spectra (at ca. 400 nm) are very similar.

Comparison of condensed phase absorption spectra with the theoretical prediction

The comparison of the recorded spectra in solution with the calculated spectra (PBE0/evGW-BSE/def2-TZVP, Figure 4) shows

a good agreement. Since solvent effects have not been included, there is better agreement with the obtained UV PD spectra in gas phase (Figure 3). The calculations show that in the excitation range of 340–355 nm, MLCT transitions or $\pi\pi^*$ transitions localized on the pyridyl-triazole residue with some MLCT character are excited (Figure 4). For energetically higher excitations, transitions of different nature are expected, where the corresponding molecular orbitals are localized on the nitrogen-containing ligand as well as on the phenyl groups of the phosphine ligand. Those energetically higher lying transitions show $\pi\pi^*$ as well as MLCT character (for a more detailed discussion, see Supporting Information chapter 13 and 14). Of interest to note is the theory-predicted but absent red-shifted band at about 400 nm of the $\text{Cu}_2\text{L}'\text{H}_2$ species. This may indicate that the calculated structure found is not the structure present in the experiment and therefore shows slightly different electronic properties. The electronic excitations of the optimized structures (gas phase) were also calculated with TDDFT, but showed a poorer agreement with the experimentally recorded spectra. (Even after the application of COSMO, a better match could be achieved, but the intrinsic problem of underestimating the energy of MLCT transitions could not be compensated (see Supporting Information chapter 14). In general, the TDDFT calculations show the same electronic transitions as the evGW-BSE calculations, but significantly red-shifted.)

Excited state dynamics on ultrafast time scale

Ultrafast pump-probe experiments were applied to study the primary processes after photoexcitation, such as FC-state relaxation, FD, IVR and ISC. Their entanglement is crucial for the formation of long-lived, functionally important states, which are then further characterized by step-scan FTIR, TCSPC and microsecond transient photodissociation (see below). In order to distinguish between matrix-related and intrinsic effects we used femtosecond UV/Vis transient absorption (fs-TA) for solution and solid phase, as well as femtosecond transient photodissociation (τ -PD) for gas phase conditions.

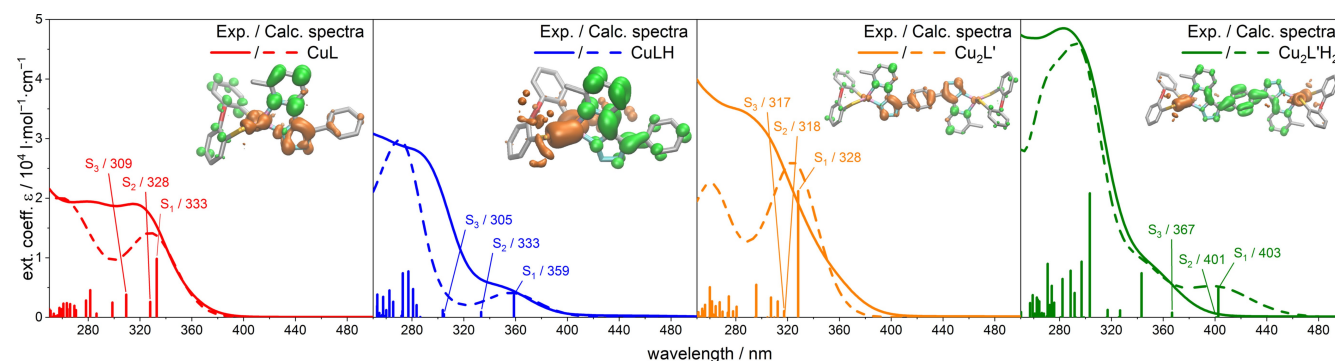


Figure 4. Comparison of static UV/Vis absorption spectra of CuL , CuLH , $\text{Cu}_2\text{L}'$ and $\text{Cu}_2\text{L}'\text{H}_2$ in DCM (solid lines) and calculated vertical transitions (dashed lines, PBE0/evGW-BSE/def2-TZVP, Gaussian convolution with $\text{FWHM} = 1500\text{ cm}^{-1}$). The transition densities of the respective S_1 states are plotted with the isovalue of $\pm 0.0015a_0^{-3}$, where green represents a gain and orange a loss of electron density. Corresponding natural transition orbitals are depicted in Figure SI-78.

Femtosecond UV/Vis transient absorption (fs-TA) in solution and solid phase

UV/Vis fs-TA experiments were performed with excitation at 350 nm. The results are shown in Figure 5 for DCM and in Figure SI-13 for solid neat film as early (a) and late (b) difference spectra, decay associated spectra (DAS) from global analysis according to Equation (3) (c), and absorbance transients with fit (d). In all samples a global, positive excited state absorption (ESA) appears within system-response, evolves on the ps-timescale and merges into a long-lived-state (with lifetime $\gg 1$ ns) absorption (A_0), identified as triplet state (T_1), which is further characterized by step-scan FTIR, TCSPC and τ -PD in the following chapters. The very similar A_4 , with $\tau_4 \approx 1$ –2 ns, is only shown for completeness and not assigned to a specific photo-

physical relaxation process. Inspection of the DAS and related time constants (see Table 2) shows that - besides specific differences discussed below - in all samples the overall spectro-temporal evolution is quite similar and well described by (similar) three processes. For the reasoning of their assignment we resort in the following to the very much resembling results on the chemically akin neutral mononuclear system [(DPEPhos)Cu(PyrTet)]^[8b] featuring a tetrazole- instead of phenyltriazolunit and a pyridyl- instead of a sterically demanding methylpyridyl-substituent. This chemical similarity is given accordingly for the mononuclear subunits of the dinuclear $\text{Cu}_2\text{L}'$ and $\text{Cu}_2\text{L}'\text{H}_2$.

(i) For the sub-ps dynamics (A_1) neither phase-state (solution vs. film) nor charge effects are observed. This strongly suggests

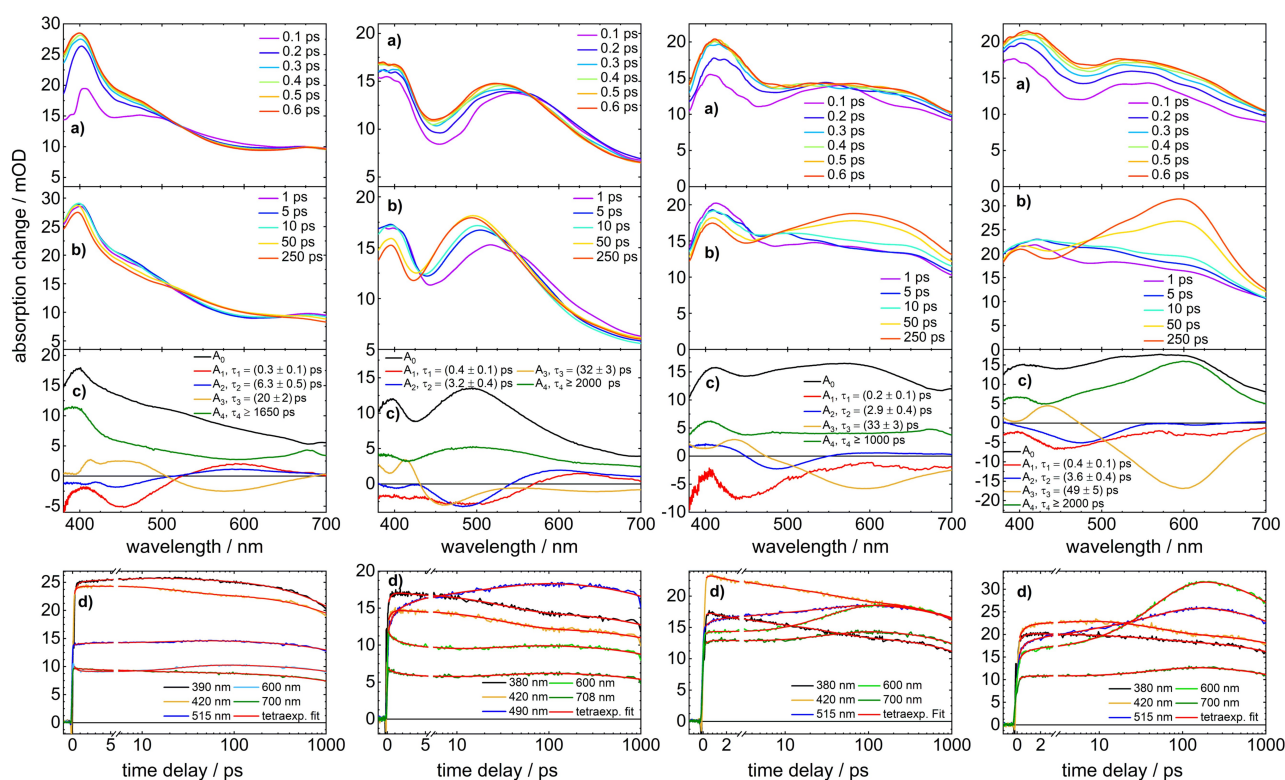


Figure 5. UV/Vis fs transient absorption of CuL (far left), CuLH (left), $\text{Cu}_2\text{L}'$ (right) and $\text{Cu}_2\text{L}'\text{H}_2$ (far right) in DCM. Excitation at 350 nm. (a) Sub-ps difference spectra; (b) 1–250 ps difference spectra; (c) DAS; (d) Absorbance transients at specific wavelengths with tetraexponential fit. Data in (a) and (b) are smoothed via 10-point FFT-filter.

Table 2. Static absorption properties and excited state dynamics, obtained by ultrafast spectroscopy of CuL, CuLH, $\text{Cu}_2\text{L}'$ and $\text{Cu}_2\text{L}'\text{H}_2$ in solution and film, and of $[\text{CuLH}]^+$, $[\text{Cu}_2\text{L}'\text{H}]^+$ and $[\text{Cu}_2\text{L}'\text{H}_2]^{2+}(\text{PF}_6)^-$ in gas phase, at $\lambda_{\text{pump}} = 350$ nm.

Complex	ext. coeff. in CH_2Cl_2 at 350 nm/ $10^3 \text{ M}^{-1}\text{cm}^{-1}$	CH_2Cl_2 solution/ps gas phase/ps				neat film/ps			
		τ_1	τ_2	τ_3	τ_4	τ_1	τ_2	τ_3	τ_4
CuL	6.9 ± 0.3	0.3 ± 0.1	6.3 ± 0.5	20 ± 2	≥ 1650	0.10 ± 0.06	3.2 ± 0.5	20 ± 3	≥ 300
CuLH	4.3 ± 0.8	0.4 ± 0.1	3.2 ± 0.4	32 ± 3	≥ 2000	0.2 ± 0.1	6.5 ± 0.7	48 ± 5	≥ 650
$[\text{CuLH}]^+$	–	0.7 ± 0.1	–	–	> 800	–	–	–	–
$\text{Cu}_2\text{L}'$	10.5 ± 0.7	0.2 ± 0.1	2.9 ± 0.4	33 ± 3	≥ 1000	0.2 ± 0.1	4 ± 1	25 ± 4	≥ 600
$\text{Cu}_2\text{L}'\text{H}_2$	$9.1 \pm 1.4^{[a]}$	0.4 ± 0.1	3.6 ± 0.4	49 ± 5	≥ 2000	–	–	–	–
$[\text{Cu}_2\text{L}'\text{H}]^{[b]}$	–	< 0.1	7.2 ± 0.7	–	> 800	–	–	–	–
$[\text{Cu}_2\text{L}'\text{H}_2]^{2+}(\text{PF}_6)^-$	–	0.26 ± 0.03	6.0 ± 0.4	–	> 800	–	–	–	–

[a] refinement with respect to Bizzarri et al.^[14] [b] species observed as deprotonation product in gas phase from $[\text{Cu}_2\text{L}'\text{H}_2]^{2+}$.

Table 3. Photophysical properties of the long-lived excited states of CuL, Cu₂L', CuLH and Cu₂L'H₂.

Complex	λ_{em} / nm		$\tau_{em} / \mu\text{s}$			$\tau / \mu\text{s}$ (amplitude)	$\Phi / \%$	
CuL	CH ₂ Cl ₂ /Ar	KBr, 290 K	KBr, 10 K	CH ₂ Cl ₂ /Ar	KBr, 290 K ^[a]	KBr, 5 K ^[a]	gas phase	CH ₂ Cl ₂ /Ar
	555	520	516	1.8	12	203	–	7
CuLH	554 ^[14]	500	507	0.9 ^[14]	20	234	2 (55%)	5 ^[14]
							18 (45%)	
Cu ₂ L'	564	519	511	2.9	44	64	–	10
Cu ₂ L'H ₂	556 ^[14]	519	536	2.8 ^[14]	9.4	225	–	14 ^[14]

[a] Given values are average lifetimes τ_{av} .

a relaxation process, which is not significantly influenced by the molecular environment. Thus, A₁ ($\tau_1 \approx 0.3$ ps) is assigned to Franck-Condon (FC) state dynamics via intramolecular vibrational relaxation or internal conversion.

(ii) For [(DPEPhos)Cu(PyrTet)]^[8b] A₂ (τ_2) has been associated with flattening distortion (FD of ca. 40°), accompanied by vibrational relaxation respectively cooling on the same, early ps-timescale. This was based on mid-IR fs-TA and UV/Vis anisotropy experiments (directly measuring the viscosity dependent angular evolution of the corresponding transition dipole moments), a pronounced spectral difference between solution and solid film (significantly hindered FD in the latter), as well as TDDFT calculations.

In fact, our TDDFT calculations predict for both mononuclear complexes FD in the relaxed S₁ state (Tables 4 and SI-9), the small magnitude of which can be related to the sterically demanding methyl group.^[29] Note that for [(DPEPhos)Cu(PyrTet)] in solution, FD has been associated with a spectral blue-shift of the ESA on the early ps-timescale.^[8b] We do not observe such a blue-shift for the four complexes, possibly due to their small FD as compared to [(DPEPhos)Cu(PyrTet)].

Further, mid-IR investigations on [(DPEPhos)Cu(PyrTet)] revealed characteristics of vibrational cooling (VC) on the same time scale, suggesting the same process for the four complexes. Thus, based on phase state characteristics (see below) of CuL, CuLH and Cu₂L', as well as TDDFT calculations on the monomers and the reports on [(DPEPhos)Cu(PyrTet)] we assign A₂ ($\tau_2 \approx 3$ –6 ps) to FD in solution in combination with VC.

Table 4. Calculated dihedral angles [°] between the planes defined by P–Cu–P and N–Cu–N (DFT/B3LYP-D3(BJ)/def2-TZVP). Flattening angles compared to the S₀ state are given in brackets, with the angles of both Cu moieties for Cu₂L' and Cu₂L'H₂. For the T₁ states of these dinuclear systems both the symmetric and the asymmetric structures are listed, including the relative energies.

Complex	S ₀ (B3LYP)	T ₁ (TDDFT/B3LYP)	T ₁ (UDFT/B3LYP)	S ₁ (TDDFT/B3LYP)
CuL	90.6	89.9 (-0.7)	89.9 (-0.7)	73.7 (-16.9)
CuLH	92.8	84.2 (-8.6)	81.0 (-11.8)	80.3 (-12.5)
Cu ₂ L'	89.6	–	91.7/91.7 (2.1/2.1)	–
			(sym., 0 kJ/mol)	
Cu ₂ L'H ₂	91.3	–	78.3/90.2 (-11.3/0.6)	–
			(asym., 30.9 kJ/mol)	
			92.5/81.5 (1.2/-9.8)	–
			(asym., 0 kJ/mol)	
			89.9/89.9 (-0.4/-0.4)	
			(sym., 19.7 kJ/mol)	

Considering the similarity of all four A₂, this assignment holds equally for both monomers and dimers.

The rigidity of the solid state counteracts large amplitude distortions^[30] and changes VC characteristics, reflected by the altered A₂. Due to the comparatively small FD amplitude predicted for CuL and CuLH in S₁, FD (or its onset) may occur in solid state as well, however, in different extent compared to solution.

(iii) A₃ ($\tau_3 \approx 20$ –50 ps) describes the formation of a long-lived excited state, which is reasonable for triplet states. Experimental^[8a] and theoretical^[31] studies on [(DPEPhos)Cu(PyrTet)] made an unambiguous assignment of ISC to this time scale. Furthermore, the similarity of A₃ in the dynamics of the neutral [(DPEPhos)Cu(PyrTet)]^[8b] with those of the four complexes (in particular of the neutral CuL) is obvious. Thus, based on the formation of a long-lived state with τ_3 and literature reports on the very similar complex [(DPEPhos)Cu(PyrTet)], A₃ (τ_3) is assigned to ISC for the four complexes. However, ultrafast ISC on the sub-ps timescale as suggested by a theoretical investigation cannot be excluded.^[32] Influences of charge and nuclearity are discussed below.

Although charge, nuclearity and phase are not observed to alter the spectro-temporal evolution (and thus the described processes) dramatically, they do lead to variations that are discussed in context with the respective processes in the following.

(i) The only (small) differences of A₁ in all samples concern negative or positive sign above ca. 550 nm. Among the solution samples, the dinuclear systems show negative, the mononuclear systems positive sign. All solid samples show positive sign, irrespective of being mono- or dinuclear, charged or neutral. Thus, FC-relaxation appears basically unchanged with respect to charge, nuclearity and phase, with phase possibly having the strongest impact.

(ii) The TDDFT calculations predict the strongest (but small) FD for CuL in the relaxed S₁ (-16.9°, Table 4) and, interestingly, its complete reversal in the relaxed T₁ (-0.7°). At first sight, the results of GW/BSE calculations of the ground state, predicting predominantly $\pi\pi^*$ character for S₁ excitation (Figure 4, Table SI-13), appear contradictory to the occurrence of FD (requiring MLCT). However, one can expect that small structural fluctuations may alter the electronic transitions significantly (see S₀ and S₁ geometries in Table SI-13), thereby changing the

character from predominantly $\pi\pi^*$ to predominantly MLCT,^[33] enabling FD and its reversal with ISC. For **CuL** the strong influence of the molecular structure on the electronic states is also exemplified by TDDFT calculations on the triplet manifold, where small alterations of the FD angle converge to three energetically close-lying structures (within 16 kJ/mol, Table SI-19), with either $\pi\pi^*$ or MLCT character (Figure SI-89 and SI-91). In contrast, for **CuLH** only one structural minimum (with clear MLCT character, see Figure SI-93, Table SI-13) was identified.

The result of the TDDFT calculations on **CuL** (FD and its reversal, Table 4) correlates well with the nearly mirror-image of A_2 and A_3 , solely observed for **CuL** among all solution samples. For the neutral system the reversal of FD could reflect a formally (partial) reduction from Cu(II) to Cu(I) in the excited MLCT state (charge backdonation). In contrast, the protonated ligands of **CuLH** and **Cu₂L'H₂** are more electronegative and thus they are less prone to backdonate (stabilizing MLCT character). In agreement, the CV data show a lower oxidation potential for the neutral complexes, since the negatively charged ligand stabilizes the oxidized Cu atom (Cu(II)) by a charge donation (see Electrochemical properties) - already without a MLCT-induced additional ligand-centered negative charge. This is the case for **CuL**.

For the dinuclear **Cu₂L'**, a comparable process is not suggested by fs-TA data. Due to the difficulties with optimizing S_1 structures of the dinuclear complexes at the TDDFT level (see Quantum chemical calculations), theoretical predictions must be taken with care. For the dinuclear complexes, LC (**Cu₂L'**) or MLCT (**Cu₂L'H₂**) vertical transitions are predicted (GW/BSE level, see Supporting Information chapter 13) and thus a clear effect on occurrence of FD is expected, in addition to altered relaxations pathways in general. Interestingly, despite the different predicted transitions, the fs-TA measurements revealed nearly identical spectra (Figure 5) in solution. This astonishingly high similarity strongly suggests that the same electronic relaxation processes take place in both dimers (neutral and charged) in solution, independent of the predicted LC (**Cu₂L'**) and MLCT (**Cu₂L'H₂**) excitation. Hence, due to the very floppy character of the dimers and the high similarity of the fs-TA data we assume that different structures are present in equilibrium in solution in a quite similar ratio for both dimers. The general

structural flexibility of the dimers seems to be reflected by the phase dependencies observed for **Cu₂L'**.

(iii) ISC (τ_3) appears to be slower in the dinuclear systems (when systems with same charge are compared) for both solution and solid phase, possibly owed to conjugation expansion^[34] in the dinuclear systems. In addition, the charged systems show a slightly slower ISC (when systems with same nuclearity are compared), for both solution and solid phase. The reason is possibly a reduced influence of spin-orbit coupling on ISC, due to a more efficient separation of the electron from the copper atom, which seems conceivable when taking solely the electrostatic properties of the nitrogen-ligand into account. Further support for the significant participation of the copper atom on ISC is given by TDDFT calculations (on the monomers). In the S_1 -state both monomers reveal FD which persists in the triplet state solely for the charged monomer and not for the neutral one (reversal FD). This implies an effective reduction of Cu(II) to Cu(I) in the neutral system. Consequently, the stronger influence of the copper atom on ISC seems evident for the neutral systems.

Femtosecond transient photodissociation (τ -PD) in gas phase

UV pump-NIR probe τ -PD spectroscopy^[35] was conducted on the isolated ionic complexes **[CuLH]⁺**, **[Cu₂L'H]⁺** and **[Cu₂L'H₂]²⁺(PF₆)⁻** in an ion trap mass spectrometer (with time delays up to 800 ps and the pump wavelength set to 350 nm), whereas the probe wavelength was fixed at 1200 nm for multiphoton excitation and fragmentation. An important prerequisite for obtaining transients by this method, however, is that the interrogation by the probe pulse should lead to different fragmentation efficiencies (or different fragment species) for the primary electronically excited state in comparison to the subsequently reached states, which are produced by (electronic) relaxation processes, for example IC or ISC.^[35b,36] Characteristic transients of the three species for a maximum time delay of 180 ps are displayed in Figure 6, kinetic fit results are given in Table 2. Additionally, transients for different maximum time delays are presented in Figures SI-14–SI-21.

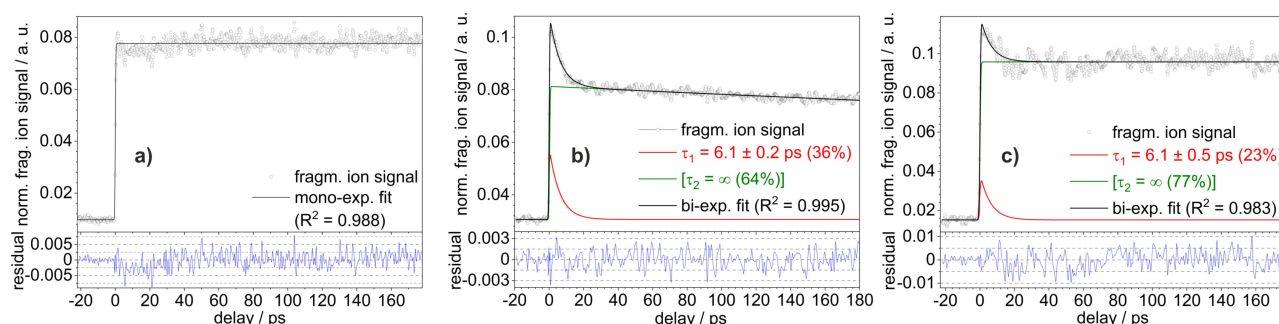


Figure 6. Normalized transient fragmentation ion intensity of a) **[CuLH]⁺**, b) **[Cu₂L'H]⁺** and c) **[Cu₂L'H₂]²⁺(PF₆)⁻** for a 200 ps time delay window with $\lambda_{\text{pump}} = 350$ nm at 0.3 μJ and $\lambda_{\text{probe}} = 1200$ nm at 130 μJ .

The τ -PD data on $[\text{CuLH}]^+$ (Figure 6, a) show after photo-excitation mainly the fast population of a long-living excited state (> 800 ps). A closer look in the 10 ps and 2 ps time delay windows (Figure SI-14) reveals possibly low-frequency wave packet modulations (with an oscillation period of ca. 1 ps, associated with a frequency of ca. 30 cm^{-1}). The τ -PD trace was fitted so that the amplitude of the chosen function was adjusted with a damped sine curve in order to fit the oscillatory behavior. The resulting damping time constant (0.7 ± 0.1 ps), which, however, can only be estimated with large uncertainty, correlates with the fast time constants found in solution (0.4 ps) and in film (0.2 ps; Table 2). The according wavepacket motion could relate to some low-frequency large amplitude relaxation, for example flattening distortion (FD), which was recently observed by optical and X-ray spectroscopy in solution for copper phenanthroline complexes to dephase in the sub-ps regime, but showing higher vibrational frequencies than observed here.^[21a,37] For the related $[(\text{DPEPhos})\text{Cu}(\text{PyrTet})]$ complex FD was found on a longer time scale of a few ps.^[8b] However, no additional time constants were found here in gas phase in longer 1–50 ps time delay windows. A possibility, which we cannot completely exclude, is that intermediate time constants (as observed in TA solution dynamics, see above) relate to states with low contrast in probe amplitude and elude our τ -PD analysis technique (see discussion above). However, since we have no further indications for such an assumption, we conclude that in gas phase a very fast decay of the primary excited state (presumably by FD/IVR/ISC) is followed up by population of a long-living state (possibly of triplet character), which points, upon comparison of the related solution dynamics by TA, towards a strong acceleration of ISC rate in gas phase. A similar behavior was recently observed for the photo-dynamics of the dinuclear platinum metal complex $[\text{Pt}_2(\text{pop})_4\text{H}_2]^{2-}$ ($\text{pop} = \text{P}_2\text{H}_5\text{O}_2^{2-}$) in gas phase^[38] and discussed in terms of closing the “dissipation-to-solvent” channel and the increase of ligand backbone flexibility, both of which should increase the ISC rate in gas phase.

The transient photodissociation data of $[\text{Cu}_2\text{L}'\text{H}]^+$ (Figure 6b) exhibit a very short time constant (< 0.1 ps) and an intermediate time constant (~ 6 ps) leading again towards a long-living state. These data agree acceptably with time constants from transient absorption (TA) measurements for $[\text{Cu}_2\text{L}'\text{H}_2]^{2+}$ obtained in solution (DCM) (0.4 ps and 3.6 ps), where additionally a third time constant of ~ 49 ps was found and assigned to ISC in comparison to former results on structurally similar copper complexes (see above).^[8b] In gas phase we would assign tentatively the sub-ps time constant to IVR (possibly also FD) and the ~ 6 ps time constant to ISC, clearly slower than in the monomeric complex $[\text{CuLH}]^+$, which could also result from increased conjugation of the dimer.^[34] Moreover, the τ -PD measurements implicate (also in agreement with the TA results from condensed phase dynamics) that a longer-living excited state (> 800 ps) exists. Its long intrinsic lifetime was obtained by a new ns pump/fs probe setup and gave a decay in the μs regime (see Microsecond transient photodissociation (τ -PD) in gas phase).

Finally, the transient photodissociation data of $[\text{Cu}_2\text{L}'\text{H}_2]^{2+}(\text{PF}_6)^-$ (Figure 6c) reveal a very similar dynamical behavior as the just presented deprotonated $[\text{Cu}_2\text{L}'\text{H}]^+$ species. From the fitting analysis of the τ -PD transients we obtain again a fast sub-ps time constant (0.26 ps) and an intermediate constant (6.0 ps). Eventually a long-living state is formed which decays only in the μs regime. Thus, here also agreement with the first two time constants from solution dynamics is observed. However, also here we would assign a clear acceleration of ISC, although it is slower than for the monomeric complex $[\text{CuLH}]^+$.

In summary, all three ionic species show in gas phase the fast population of a long-living state, presumably a triplet state, consistent with the overall observations of dynamics in condensed phase. The intermediate dynamics (in the few ps and few tens of ps regime) obtained in solution are hardly observed in the gas phase. Only a time constant of ~ 6 –7 ps was revealed for the dinuclear species. So, we conclude that i) solvent relaxation (and energy transfer to solvent) is involved in these ps processes and ii) ISC dynamics are strongly accelerated in gas phase for all species, where the ISC rate seems to be slower for the dinuclear ($[\text{Cu}_2\text{L}'\text{H}]^+$, $[\text{Cu}_2\text{L}'\text{H}_2]^{2+}(\text{PF}_6)^-$) vs. the mononuclear ($[\text{CuLH}]^+$) complexes. The same qualitative dependence on nuclearity was found for the condensed phase ultrafast dynamics.

Excited state dynamics on the nano- and microsecond time scale

Luminescence in solution and solid phase

As ultrafast spectroscopy evidenced long-lived excited states with lifetimes of nanoseconds or longer, static and time-resolved luminescence spectroscopy was applied to analyze potential emissions. Indeed, all four complexes show luminescence in the solid state (KBr matrix, neat film) and in solution (CH_2Cl_2) after UV excitation. Broad emission bands centered at 555–500 nm are observed, depending on the complex and the medium (Table 3), which are common values for Cu(I) complexes with emissive MLCT states.^[1c,5,14,16b] The emission maxima in CH_2Cl_2 (Figure SI-28, Table 3) are red-shifted by up to 64 nm compared to the solid state (KBr matrix) luminescence (Figure SI-29, Table 3), which may be explained by a more efficient structural relaxation in the electronically excited state in the liquid phase (see also respective discussion on FD in solution vs. solid media in the fs-TA section).^[12a,30] At the same time, the emission maxima in solution are almost unaffected by the charge and the nuclearity of the complexes. However, the impact is much larger in the solid state (KBr matrix) with, for example the emission maximum of CuLH being blue-shifted by 19 nm and 29 nm as compared to $\text{Cu}_2\text{L}'\text{H}_2$ at 290 K and 10 K, respectively (see below and Table 3). Similar results were obtained in the solid phase by probing neat films (Figure SI-30), so that the influence of KBr is insignificant here.

The effects of charge and nuclearity on the luminescence energy (via the respective emission maxima) can be considered

in the sense of two body cooperativity^[39] by applying the following Equation (1):

$$\Delta E_{\text{coop}} = E(\text{Cu}_2\text{L}'\text{H}_2) - E(\text{Cu}_2\text{L}') - 2(E(\text{CuLH}) - E(\text{CuL})) \quad (1)$$

Interestingly, the values for ΔE_{coop} are not equal to zero in all the studied media and amount to absolute values of up to 1600 cm^{-1} in the solid state at 10 K (see below), which is a contribution of 8% (Table SI-4). The ΔE_{coop} values in the solid phase are throughout negative, while positive numbers are obtained in CH_2Cl_2 . This means that the effects of charge and nuclearity on the emission properties are not additive, indicating negative (solid state) and positive (CH_2Cl_2) cooperative effects, respectively. The magnitude of the observed luminescence shifts is of the order or even larger than the effects obtained, for example experimentally for dinuclear iridium, palladium and platinum containing transition metal complexes with (2-dimethylamino)-4-(2-pyrimidinyl)pyrimidine ligands.^[39b]

The photoluminescence quantum yield amounts to 5–14% in deaerated CH_2Cl_2 with a luminescence decaying monoexponentially with a lifetime of $\tau = 0.9\text{--}2.9\text{ }\mu\text{s}$ (Table 3). In general, these values are quite high compared to related Cu(I) complexes,^[5,8c,40] which directly correlates with the throughout small flattening angles in the excited state (Tables 4 and SI-9, see also fs-TA and step-scan FTIR spectroscopy). It is important to mention that in CH_2Cl_2 the lifetimes of the dinuclear systems are longer than those of the mononuclear analogues, paralleled by higher photoluminescence quantum yields. In the solid state, the emission shows a bi- or triexponential decay with an increased average lifetime of $\tau_{\text{av}} = 9.4\text{--}44\text{ }\mu\text{s}$ (290 K) compared to the monoexponential decay constants in solution (Table 3). This increase from the liquid to the solid phase may be explained by the absence of non-radiative deactivation channels via solvent molecules in the KBr matrix and the smaller excited state distortions in the more rigid medium further slowing down non-radiative deactivations.^[12a,30] The average decay constant τ_{av} was calculated by considering the time constants τ_1 , τ_2 (and τ_3) with their relative contributions (Eq. (4)),

where one should be aware that τ_{av} is appropriate to discuss relative trends, but cannot be directly assigned to one specific excited state. In detail, the emission decay in the solid state is composed of two dominating ($\geq 80\%$ in total) long-lived components of several microseconds (up to $94\text{ }\mu\text{s}$ in KBr at 290 K, Table SI-5). The bi- or triexponential decay in the solid state might result from contributions of energetically higher substates or different microenvironments (e.g. distance to counter ions, packing effects, solvent molecules in the crystal lattice) in the solid sample. Considering the literature reports on related Cu(I) complexes, two separate long-lived triplet states are less likely due to a fast spin-lattice relaxation between the triplet sublevels at 290 K^[16a,41] and at the same time a potential thermally activated delayed fluorescence mechanism (see below) does rather not involve two distinct excited triplet states, at least in the solid state.^[13] This means that two different excited states in one molecule are improbable with respect to the literature. However, the biexponential decays on the microsecond time scale observed in the gas phase by transient photofragmentation rather indicate two different electronically excited (micro)states (see Femtosecond transient photodissociation in gas phase), so that this point can unfortunately not be fully answered by the applied time-resolved methods.

The above mentioned average emission lifetime of $\tau_{\text{av}} = 9.4\text{--}44\text{ }\mu\text{s}$ at 290 K could be assigned either to phosphorescence or delayed fluorescence. In the literature many reports on Cu(I) complexes describe thermally activated delayed fluorescence (TADF) at room temperature by an efficient reverse intersystem crossing from the lowest excited triplet state to the lowest excited singlet level and subsequent delayed fluorescence to the electronic ground state.^[5,16, 42] To achieve a deeper understanding for potential thermally activated deactivation processes, temperature-dependent static and time-resolved luminescence investigations were performed on KBr pellets. Cooling of KBr samples of the four complexes to 170 K/130 K red-shifts the static emission spectrum by $250\text{--}780\text{ cm}^{-1}$, which is characteristic for the inhibition of a TADF mechanism at lower thermal energy and phosphorescence from the triplet state T_1 (Figures 7 and SI-31–SI-33). Surprisingly, this initial red-shift turns into a blue-shift of $210\text{--}720\text{ cm}^{-1}$ when the sample is

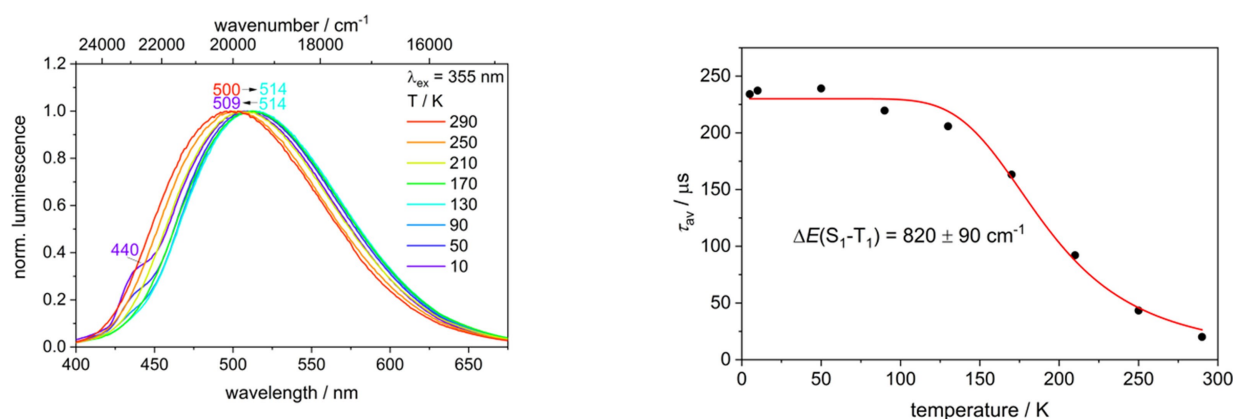


Figure 7. Static emission spectra of CuLH in a KBr matrix at 10–290 K (left). Average lifetime τ_{av} of CuLH at temperatures of 5–290 K (right).

further cooled down to 10 K. Hence, this indicates two opposite effects at low temperature. The blue-shift may result from an inhibited excited state relaxation at low temperature, which is termed as “rigidochromism” in the literature.^[43] Indeed, this effect is typical for ³MLCT states and is definitely conceivable for the emissive triplet states (see following section on temperature dependent luminescence lifetimes) of the four complexes.

The blue-shift may be smaller for **CuLH/Cu₂L'H₂** as a result of their higher intrinsic flexibility (see fs-TA in the condensed phase, step-scan FTIR spectroscopy and DFT calculations). Beside the described spectral shifts, pronounced shoulders appear at temperatures of ≤ 50 K, particularly for **CuL** (Figure SI-31). These shoulders are separated by approx. 1000 cm⁻¹ and are assigned to a vibrational progression. Indeed, the measured FTIR ground state spectrum reveals several vibrations around 1000 cm⁻¹ (Figure SI-43).

For a deeper elucidation of the radiative deactivation mechanisms, time-resolved luminescence studies were performed at temperatures down to 5 K. Interestingly, the average luminescence lifetime τ_{av} increases sharply between approximately 250–130 K by a factor of approx. 7–9 to values of $\tau_{av} = 203$ –234 μ s (5 K) for **CuL**, **CuLH** and **Cu₂L'H₂** (Figures 7, SI-35 and SI-37). This should result from a significant contribution of thermally activated delayed fluorescence at room temperature and a steadily growing contribution of long-lived phosphorescence from the T₁ state at low temperature. Assuming that the S₁ and T₁ states are in thermal equilibrium, the following equation^[16a] can be considered to get an estimation of the energy separation ΔE between the T₁ and S₁ states:

$$\tau(T) = \frac{3 + \exp(-\frac{\Delta E}{kT})}{\frac{3}{\tau(T_1)} + \frac{1}{\tau(S_1)} \exp(-\frac{\Delta E}{kT})} \quad (2)$$

where kT is the thermal energy, $\tau(S_1)$ and $\tau(T_1)$ are the intrinsic fluorescence and phosphorescence lifetimes and the factor 3 is introduced to consider three triplet substates. The experimental temperature-dependent trend of τ_{av} can be very well fitted with Equation (2) with energy barriers of 800–960 cm⁻¹ for **CuL**, **CuLH** and **Cu₂L'H₂**. The observations for the temperature dependent evolution of the luminescence lifetimes and the deduced energy gaps ΔE (800–960 cm⁻¹ according to Equation (2)) correlate with the spectral red-shifts (550–780 cm⁻¹) observed upon cooling from 290 K to 170/130 K (Table SI-6). The slightly lower values obtained from the static spectra should result from the blue-shift at low temperature. Overall, the experimental ΔE values are similar to the S₁–T₁ gaps of related complexes reported in the literature.^[5] However, the experimental values are lower than those obtained by the DFT/PBE0 and DFT/B3LYP calculations for the mononuclear systems (Tables SI-11 and SI-18). Furthermore, the fit based on Equation (2) gives an approximation of the intrinsic S₁ and T₁ lifetimes $\tau(S_1)$ and $\tau(T_1)$ amounting to 40–170 ns and 180–230 μ s, respectively (Table SI-5). Interestingly, $\tau(T_1)$ is slightly higher for the dinuclear system **Cu₂L'H₂** compared to the mononuclear analogue **CuLH**, in analogy to the lifetimes observed in CH₂Cl₂ solution (Table 3). This correlation might

indicate pure phosphorescence in solution, which may result from increased S₁–T₁ energy gaps.

In contrast to the three systems **CuL**, **CuLH** and **Cu₂L'H₂** with strongly temperature dependent luminescence lifetimes, the average time constant of **Cu₂L'** only increases by approx. a factor of 1.5 with a high value of $\tau_{av} = 44$ μ s at 290 K (Table 3, Figure SI-36), so that Equation (2) is not applicable. This indicates efficient phosphorescence also at 290 K in the solid state and at most a small contribution of TADF. Hence, the photoluminescence behavior of **Cu₂L'** strongly differs from the emission properties of the other three complexes, which can also be understood as a kind of cooperative effect. The absence of (efficient) TADF also explains the very small spectral red-shift of only 250 cm⁻¹ upon cooling, which does not necessarily result from a suppression of a TADF process.

Considering the full picture of the luminescence properties in the condensed phase, charge and nuclearity do not have a systematic influence on emission maxima and lifetimes (including intrinsic time constants). At the same time, it was observed that the effects are clearly not additive with respect to charge and nuclearity, so that they could be evaluated in the sense of two-body cooperativity. The most surprising point is that the temperature-dependent behavior is significantly different for **Cu₂L'**, which may be explained by an efficient phosphorescence combined with a very moderate reverse intersystem crossing at room temperature. In the next step, we move to the analysis of the long-lived electronically excited states in the gas phase to achieve further information on their intrinsic properties.

Microsecond transient photodissociation (τ -PD) in gas phase

In order to complement the luminescence lifetime data of the preceding paragraph, we evaluate now the intrinsic electronic lifetimes, i.e. lifetimes of the isolated chromophore units without interaction with solvent molecules, counter ions or matrix environment, on the microsecond time scale. This investigation serves to verify the assignment of electronic states, assess environmental influences and excludes processes like excimer or exciplex formation and can, naturally, only be achieved under gas phase conditions. Therefore we utilized an upgraded laser setup (see Experimental Section), where an additional ns kHz OPO laser was synchronized with the existing femtosecond laser system, it is now possible to perform excited state lifetime measurements by transient pump-probe photodissociation (τ -PD) for long-living states, for example triplets, employing (electronically scanned) time delays in the ns-ms regime.^[44] This novel approach is of special interest for non-luminescent, isolated systems which can hardly be interrogated otherwise for their intrinsic lifetimes.

The complex cation **[CuLH]⁺** was thus investigated by ns pump (350 nm)/fs probe (1200 nm) with a time resolution of ca. 50 ns and a time delay of up to 200 μ s. The τ -PD result (Table 3) shows a biexponential decay for **[CuLH]⁺** (~2 μ s, ~18 μ s) as displayed in Figure 8. Unfortunately, we could not study the **[Cu₂L'H]⁺** and **[Cu₂L'H₂]²⁺(PF₆)⁻** complex using this technique due to too small ns pump/fs probe contrast signal. The lifetimes

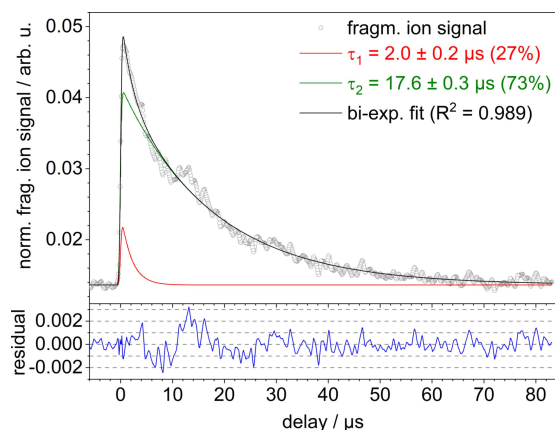


Figure 8. Normalized transient fragmentation ion intensity of $[\text{CuLH}]^+$ for a 90 μs time delay window; ns pump (350 nm, 1 μJ) and fs probe (1200 nm, 130 μJ) experiment.

for $[\text{CuLH}]^+$ are clearly longer than the results from DCM solution and correspond well to results obtained by TCSPC luminescence ($[\text{CuLH}](\text{BF}_4)$, 290 K, KBr matrix; Table 3) of 20 μs as recorded at the slightly longer excitation wavelength of 390 nm.

In summary, using a new ns/fs pump-probe τ -PD setup we were able to obtain the intrinsic μs lifetime of a photocatalytically active ionic species under isolated conditions in an ion trap mass spectrometer. The results give strong support for a long-lived excited state (triplet state), point towards significant quenching in DCM solution and relate relatively well to luminescence lifetimes in KBr matrix for $[\text{CuLH}]^+$.

Structural characterization of the long-lived excited states in solid phase by step-scan FTIR

Subsequent to the clear evidence of long-lived (microseconds) excited states in the time-resolved luminescence and photo-fragmentation (gas phase) studies, which are populated after UV excitation and femtosecond deactivation processes (see fs-TA spectroscopy in the condensed and gas phase), we conducted step-scan FTIR experiments to analyze the structures of the long-lived electronically excited states. The step-scan technique has previously been successfully applied to transition metal complexes,^[45] including the structural characterization of di- and tetranuclear Cu(I) complexes.^[46]

Prior to the step-scan FTIR investigations, ground state FTIR spectra of solid samples (KBr pellets) were recorded at 20 K and 290 K. The ground state FTIR spectra of the four compounds are very similar (Figure SI-42), as the differences mostly result from the absorption of the BF_4^- counterion at 1250–950 cm^{-1} (see IR spectrum of NaBF_4 in KBr as a reference for the anion, Figure SI-51) in case of the charged systems CuLH and $\text{Cu}_2\text{L}'\text{H}_2$ (Figure SI-42). Furthermore, the ground state IR absorption is hardly influenced by temperature (Figures SI-43–SI-46). The experimental ground state spectra are in very good agreement with the calculated IR spectra (B3LYP-D3(BJ)/def2-TZVP), where one

should be aware that the counter ions were not considered in the calculations for the protonated species (Figures 9, SI-47–SI-50). The theoretical spectra enabled the assignment of the different absorption bands to specific vibrations, which are for the most part delocalized (Tables SI-7 and SI-8).

The samples were then excited with a 355 nm UV laser pulse at 20 K and 290 K to measure step-scan difference spectra (Figures SI-52–SI-59) and thus analyze small but nevertheless significant vibrational changes in the solid medium. In these difference spectra, averaged over the first microsecond after laser excitation, the peaks pointing in negative direction are almost identical to the corresponding vibrations in the electronic ground state and result from the depopulation of the electronic ground state. At the same time, the peaks pointing in positive direction are assigned to the populated long-lived electronically excited states. It should be mentioned here that the difference spectra show a compound specific positive offset of unclear origin, so that also the Δ absorbance values of the negative peaks are mostly positive. For this reason, no reliable excited state lifetimes could be extracted from the step-scan data in this particular case. Nevertheless, it is obvious from the transient FTIR data that the complexes show lifetimes of at least several microseconds at 290 K and 20 K in the solid state, in full agreement with the time-resolved luminescence experiments in solid phase (see also microsecond τ -PD). This underlines that the lowest excited triplet state is probed in the step-scan FTIR experiments. Note that also at 290 K with occurrence of a TADF mechanism mainly the lowest triplet state T_1 should contribute

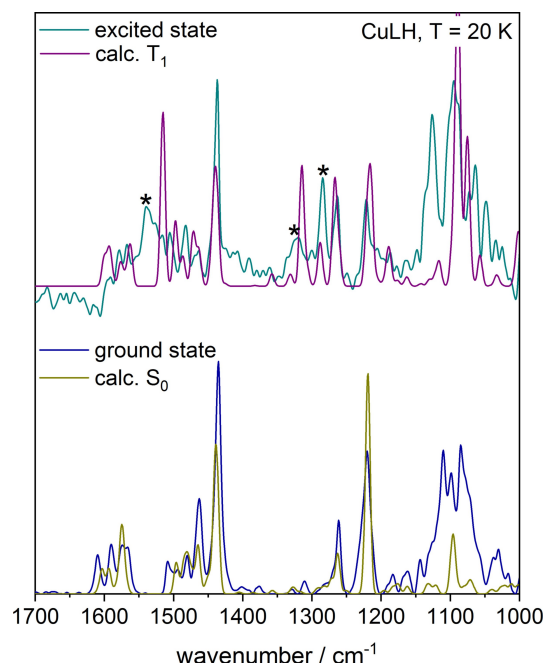


Figure 9. Excited state IR spectrum (1.0% of the ground state spectrum added to the step-scan difference spectrum) and calculated T_1 spectrum of CuLH (top). Static FTIR ground state spectrum (KBr pellet, 20 K) and calculated S_0 spectrum of CuLH (bottom). Calculations: (TD-)DFT/B3LYP-D3(BJ)/def2-TZVP, scaled by 0.975, FWHM = 8 cm^{-1} , Gaussian profile. The bands marked with asterisks are discussed in the text.

to the step-scan spectrum, as the intrinsic lifetime of the S_1 state is much shorter (see luminescence spectroscopy).

For a better direct comparison between the IR absorption in the electronic ground state and in the electronically excited state the pure excited state IR absorption spectra were generated by addition of 0.5–2.0% (depending on the sample and temperature) of the ground state spectrum to the step-scan difference spectrum to compensate the negative bands (Figures SI-60–SI-63). The low ground state contribution results from the small number of molecules in the pellet excited by each laser pulse. The obtained excited state IR spectra can then be directly compared to the corresponding ground state spectra, where it is observed that strong excited state specific peaks are observed for **CuLH** (Figure SI-60) and **Cu₂L'H₂** (Figure SI-63). The mentioned peaks are observed at wavenumbers where the IR absorption in the electronic ground state is much weaker or even completely absent. For instance, these bands are localized at 1539, 1320 and 1285 cm^{-1} for **CuLH** (see asterisks in Figure 9). Excited state specific features of similar intensity were obtained for **Cu₂L'H₂** (see asterisks in Figure SI-63), whereas the effects were weaker for **CuL** (Figure SI-61). This is a first indication for smaller geometrical distortions in the excited triplet state for **CuL** (see below). Beside the investigations in the KBr matrix, **Cu₂L'H₂** was measured as neat film with spectra very similar to those obtained in KBr, so that matrix effects are not relevant here (Figure SI-64).

Comparing the excited state IR spectra at 20 K with those recorded analogously at 290 K, it is observed that the effects are principally the same (Figures SI-60–SI-63). However, the excited state specific features are weaker at 290 K compared to 20 K, which may result from the coupling of vibrational modes in the region of approx. 1700–1000 cm^{-1} with thermally populated low frequency vibrations. These couplings induce vibrational broadening, so that the transient IR absorption features are then hard to probe experimentally.

For a more profound structural characterization of the excited triplet states of the mononuclear complexes **CuL** and **CuLH**, the experimental excited state IR spectra were directly compared to the theoretical T_1 spectra. Generally, the experimental spectra are in good agreement with the corresponding calculated spectra obtained by TDDFT and UDFT (B3LYP-D3(BJ)/def2-TZVP). Interestingly, the intense excited state specific features of **CuLH** observed experimentally are very well reproduced by theory (TDDFT). Hereby, it should be mentioned that all the TDDFT optimizations with different starting structures (e.g. with different dihedral angles) converged into the same minimum structure. Analogous results were obtained by calculating the triplet state as ground state (UDFT) (Figure SI-66). Similar statements hold for **CuL** with the main difference that there are no pronounced excited state specific features, as described above (Figures SI-61 and SI-65). Furthermore, an important point is that TDDFT yielded three energetically close-lying triplet states (within 16 kJ/mol, Table SI-19), so that corresponding harmonic frequency calculations could give an even better agreement between experiment and theory, which is however beyond the focus of this work.

The good agreement between the experimental and theoretical excited state IR spectra allowed a deeper analysis of the excited triplet geometries and the underlying electronic characters, especially with respect to the flattening distortion (FD) under consideration of the change of the calculated dihedral angle between the planes defined by P–Cu–P and N–Cu–N in the excited triplet state (Tables 4 and SI-9). In the case of **CuL**, the dihedral angle is almost identical in the ground state and in the T_1 state with values of 90.6° and 89.9°, respectively (considering (TD-)DFT/B3LYP, see also UDFT in Tables 4 and SI-9). This is confirmed by the large similarities between the ground and excited state spectra observed experimentally as well as the good correlation between the experimental and calculated T_1 spectra. A different situation is observed in the case of **CuLH**, with a significant FD of 8.6° from the ground state to the triplet state. This was confirmed experimentally by the strong changes in the excited state IR spectrum compared to the ground state, in accordance with the simulated S_0 and T_1 IR spectra. Hence, the protonation of the triazole ring leads to an increased flexibility and persistent FD of the complex (**CuLH** vs. **CuL**, see also fs-TA in the condensed phase), which is explained by the efficient oxidation of Cu(I) to Cu(II) (inducing FD) and transfer of electron density to the electronegative triazole ligand. The electronegative character of the protonated systems correlates with the higher redox potentials of **CuLH** and **Cu₂L'H₂** compared to their neutral analogues (Table 1). However, the observed FDs are throughout small compared to the much larger flattening angle of 40° for the related complex [(DPEPhos)Cu(PyrTet)]^[8b] and other mononuclear Cu(I) complexes.^[5,47] For both mononuclear complexes, **CuLH** and **CuL**, the populated long-lived triplet state shows a significant MLCT contribution according to the differential electron and spin densities calculated by TDDFT and UDFT, respectively (Figures SI-88 and SI-89 for **CuL**; Figures SI-92 and SI-93 for **CuLH**, see also natural population analysis in Tables SI-12–SI-14). However, a ligand-centered $\pi\pi^*$ contribution dominates over the MLCT character for **CuL**, which should arise from the intrinsically negatively charged triazole ligand making a shift of electron density from the Cu center to the ligand less advantageous.

With respect to the dinuclear complexes, the experimental excited triplet IR spectra of **Cu₂L'** and in particular **Cu₂L'H₂** show significant differences compared to the ground state spectra indicating structural changes (Figures SI-62 and SI-63). At the same time, the excited state spectra of both complexes resemble each other, but are clearly not identical, which may result from distinct geometries even though their ultrafast dynamics are very similar (Figures SI-71 and SI-74) (see fs-TA in the condensed phase).

For the dinuclear complexes **Cu₂L'H₂** and **Cu₂L'** two different triplet minimum structures were obtained by UDFT with a symmetric and an asymmetric structure for each complex. In the symmetric triplet the FD is identical on each Cu subunit with very small changes compared to the electronic ground state of –0.4° and 2.1° for **Cu₂L'H₂** and **Cu₂L'**, respectively (Tables 4 and SI-9). The asymmetric triplets, for their part, show a much larger FD on one Cu subunit of –11.3° for **Cu₂L'** and

-9.8° for $\text{Cu}_2\text{L}'\text{H}_2$, whereas the other Cu center is mostly unaffected (Tables 4 and SI-9). Interestingly, the asymmetric triplet is energetically lower by 19.7 kJ/mol compared to the symmetric one for $\text{Cu}_2\text{L}'\text{H}_2$, while it is the other way around for $\text{Cu}_2\text{L}'$ (+30.9 kJ/mol for the asymmetric triplet) (Table 4).

Comparing the corresponding calculated IR spectra of the described triplet states with the experimental IR spectra, it is observed that the spectrum of the asymmetric triplet state of $\text{Cu}_2\text{L}'\text{H}_2$ gives a good description of the excited state specific features observed by step-scan FTIR (Figure SI-68). The theoretical spectrum of the symmetric triplet state, however, shows three intense bands in the region of $1350\text{--}1420\text{ cm}^{-1}$, which were not found experimentally. Nevertheless, as described in the introductory part on quantum chemical calculations, one should be aware of the very large conformational flexibility of the mononuclear systems, so that other triplet conformers may give an even better agreement with the experiment. Considering the currently available data set, the found asymmetric and energetically most stable triplet state with a local FD on one Cu unit is assigned to the experiment. As the spin density is mainly localized on one copper core, the pyridyl-triazole ligand and the phenyl bridge, the triplet state is of localized $^3\text{MLCT}$ character (Figure SI-103).

This discussion is less evident for the deprotonated complex $\text{Cu}_2\text{L}'$, where the calculated IR spectra of both triplet states (symmetric and asymmetric) are both in reasonable agreement with the experiment (Figure SI-67). For the symmetric and energetically lowest triplet state the strong calculated band at 1360 cm^{-1} is not obviously present in the measured excited state spectrum, but might contribute via a broad absorption to the particularly large offset in this region. Furthermore, it cannot be excluded that the very high calculated intensity of the band results partially from a methodical artefact. Finally, no unambiguous assignment of a calculated triplet state to the experiment is possible for $\text{Cu}_2\text{L}'$ by considering solely the measured and calculated IR spectra. However, the symmetric triplet state being 30.9 kJ/mol lower in energy, it is conceivable that this one is finally populated. The spin density of this triplet state is mainly localized on the pyridyl-triazole ligand and the phenyl bridge, indicating a $\pi\pi^*$ transition on the bridging ligand (Figure SI-98). The absence of a significant oxidation of a Cu center thus explains the small FD.

According to the experimental results at both 20 K (Figures SI-69–SI-70) and 290 K (Figures SI-72–SI-73), the excited state spectra of the dinuclear systems do not correspond to the sum of the spectra of the underlying mononuclear subunits, which can be attributed to a cooperative effect.

Summarizing the step-scan FTIR analysis, it should be said that the protonated mononuclear system clearly has a higher flexibility compared to the neutral one (consider FD angles, Tables 4 and SI-9) according to step-scan FTIR spectroscopy in combination with theory. Considering the dinuclear systems, it is concluded that the different triplet characters ($^3\text{MLCT}$ for $\text{Cu}_2\text{L}'\text{H}_2$ and $\pi\pi^*$ for $\text{Cu}_2\text{L}'$) and the resulting differing geometries (asymmetric for $\text{Cu}_2\text{L}'\text{H}_2$ and symmetric for $\text{Cu}_2\text{L}'$) would explain the discrepancies in the experimental excited state spectra.

Conclusion

Applying a broad range of physicochemical methods together with high-level quantum chemical calculations we here present a comprehensive photochemical and photophysical characterization of a set of closely related complexes, that build on the CuL unit with a methylpyridyl-triazole (MPyrT)/DPEPhos ligand system and differ in charge and nuclearity. Including condensed phase (solution and solid state, i.e. neat films and KBr matrix) as well as gas phase conditions, this concerted approach allows to explore - in a synoptic manner - the impact of a large variety of physical parameters on the molecular structure in the ground and electronically excited states, and their ultrafast and long-term dynamics by non-radiative and radiative, i.e. luminescent, deactivation.

In particular, our investigations demonstrate that a small variation (protonation/deprotonation) in the ligand sphere, going from the negatively charged MPyrT (in CuL) to the neutral one (in CuLH), leads to profound changes in the photochemistry and dynamics of the complexes. The mononuclear neutral CuL and cationic CuLH complexes exhibit (in part) strikingly different behavior with respect to 1) their electrochemical reactivity (strong shift to lower oxidation potential for CuL), 2) oxidative quenching, 3) electronic absorption (red-shift of CuL), 4) ultrafast dynamics (time constants and excited state spectra support flattening distortion (FD) relaxation in S_1 for CuL and CuLH but reversal of FD in T_1 for CuL) and 5) long-lived electronically excited state vibrational and structural properties (small changes for CuL but strong changes for CuLH with respect to the IR spectra of S_0 and T_1 state). However, the condensed phase luminescence spectra and lifetimes are very similar for both mononuclear complexes supporting the formation of a long-lived triplet state, with further proof for its intrinsic nature by the gas phase dynamics results, and temperature characteristics of a TADF process.

This behavior is well supported and rationalized by electronic structure calculations at TDDFT, UDFT and GW-BSE (Bethe-Salpeter equation) level for ground (S_0) and excited states (S_1 , T_1). Additionally, theory served to provide simulations for the absorption spectra of the investigated species in agreement with experimental results in gas and condensed phases and allowed for assignment of the relevant electronic transitions and vibrational modes.

It should be emphasized that the exploration and rationalization of such sensitivity on ligand-sphere modifications is highly important for applications, for example as OLEDs or photosensitizers, and should ultimately guide efficient compound optimization.

The interpretation of the results for the dimers $\text{Cu}_2\text{L}'$ and $\text{Cu}_2\text{L}'\text{H}_2$, with the latter structure revealed here for the first time, turned out to be more challenging both from an experimental and a theoretical perspective. A difference in electrochemical reactivity is observed as for the mononuclear complexes, but their absorption spectra are very similar. Moreover, the ultrafast dynamics of the dinuclear $\text{Cu}_2\text{L}'$ resemble very much those of $\text{Cu}_2\text{L}'\text{H}_2$, despite their different charge. Also, their luminescence spectra and lifetimes in solid state and solution are similar, but

from the lifetimes-temperature dependence we assigned a TADF process to $\text{Cu}_2\text{L}'\text{H}_2$, whereas only a very moderate effect of thermal energy was observed for the deactivation in $\text{Cu}_2\text{L}'$. The latter shows lower RISC efficiency than the monomer CuL , where a more effective restriction of specific vibrations via intermolecular interactions in the solid state sample may take place, as discussed by Li et al. for closely related complexes.^[48]

However, the dimers T_1 vibrational spectra show significant and distinct differences compared to the respective S_0 vibrational spectra, suggesting structural changes such as FD, yet with subtle structural differences comparing the two dimers. It is noted, that also significant differences are observed between the T_1 vibrational spectra of the mono- and the dinuclear systems. This implies that the coupling between the monomer-like units in the respective neutral or charged dinuclear system efficiently alters the (structural) dynamics observed in $\text{Cu}_2\text{L}'$ and $\text{Cu}_2\text{L}'\text{H}_2$ in a non-additive manner to a certain extent. Interestingly, from the theoretical analysis the UDFT geometry optimizations of the T_1 states of the dinuclear complexes let us expect that they would rather behave in the same manner as their mononuclear counterparts. The calculated dihedral angles in the T_1 state show no FD for $\text{Cu}_2\text{L}'$ but decent FD (ca. 10°) for $\text{Cu}_2\text{L}'\text{H}_2$ for the respective lowest energy structures. Thus, with respect to charge, FD is predicted by theory for the dinuclear systems in the same qualitative way as for the mononuclear ones. This was confirmed for $\text{Cu}_2\text{L}'\text{H}_2$ by considering the experimental and calculated T_1 spectra with the assignment of the asymmetric triplet structure (excitation on one monomeric unit) to the experiment. However, the same considerations for $\text{Cu}_2\text{L}'$ do not allow an unambiguous conclusion on this issue with the current set of calculations. Thus, it is concluded that, at the present state, the calculations do not fully support the experimental results for the dinuclear systems. Reasons for this might be found in the coexistence of conformers of the dinuclear systems in solution, respectively neat film or KBr matrix, which might alter significantly kinetic relaxation rates and pathways (e.g. branching reactions to various T states), as well as excited electronic state energies. These factors are not taken into account by the current calculations.

To sum up, there is a limited and not so clear-cut influence of charge for the dimeric complexes and we have experimentally observed some results that point towards non-additive interaction between the CuL moieties. However, a cooperative interaction is difficult to ascertain at the current level of research. On the contrary, our theoretical analysis predicts symmetry and symmetry breaking for the electronically excited states of $\text{Cu}_2\text{L}'$ and $\text{Cu}_2\text{L}'\text{H}_2$, respectively, where the former might point to some degree of cooperative interaction but reveals no structural change compared with the related monomer CuL .

Finally, we have presented here a class of four copper diimine complexes that allow for a unique study to investigate the interdependence of a great variety of photophysical and photochemical processes over nine orders of magnitude in time (scales) on both charge and nuclearity with a connection to application. We believe that the opportunities to explore the photochemistry of this compound class are not exhausted but

rather offer possibilities to tackle important questions of current (inorganic) photochemistry, like symmetry breaking in the excited state,^[49] design of efficient earth-abundant photosensitizers^[50] and cooperative interactions in multimetallic complexes^[15] in the future.

Experimental Section

Synthesis

Syntheses were performed according the literature.^[14] Experimental details are given in the Supporting Information.

Crystal structure determinations

The single-crystal X-ray diffraction of $\text{Cu}_2\text{L}'\text{H}_2$ study was carried out on a Bruker D8 Venture diffractometer with PhotonII detector at 123(2) K using $\text{Cu-K}\alpha$ radiation ($\lambda = 1.54178 \text{ \AA}$) or $\text{Mo-K}\alpha$ radiation ($\lambda = 0.71073 \text{ \AA}$). Dual space methods (SHELXT)^[51] were used for structure solution and refinement was carried out using SHELXL-2014 (full-matrix least-squares on F^2).^[52] Hydrogen atoms were refined using a riding model. A semi-empirical absorption correction was applied. The central phenyl moiety and solvent molecules CDCl_3 were disordered (see cif-files for details). $\text{Cu}_2\text{L}'\text{H}_2$: colorless crystals, $\text{C}_{94}\text{H}_{74}\text{CuN}_8\text{O}_2\text{P}_4 \cdot 2 \text{BF}_4 \cdot 8 \text{CDCl}_3$, $M_r = 2735.18$, crystal size $0.22 \times 0.18 \times 0.14 \text{ mm}$, monoclinic, space group $C2/c$ (No. 15), $a = 44.0823(10) \text{ \AA}$, $b = 10.6559(2) \text{ \AA}$, $c = 31.5479(8) \text{ \AA}$, $\beta = 125.145(1)^\circ$, $V = 12117.6(5) \text{ \AA}^3$, $Z = 4$, $\rho = 1.499 \text{ Mg/m}^{-3}$, $\mu(\text{Cu-K}\alpha) = 6.32 \text{ mm}^{-1}$, $F(000) = 5496$, $T = 123 \text{ K}$, $2\theta_{\text{max}} = 144.6^\circ$, 88283 reflections, of which 11937 were independent ($R_{\text{int}} = 0.036$), 740 parameters, 892 restraints (see cif-file for details), $R_1 = 0.092$ (for 10461 $I > 2\sigma(I)$), $wR_2 = 0.272$ (all data), $S = 1.03$, largest diff. peak / hole = 2.10 (in solvent CDCl_3) / -1.11 e \AA^{-3} . Deposition Number 2084996 ($\text{Cu}_2\text{L}'\text{H}_2$) contains the supplementary crystallographic data for this paper. These data are provided free of charge by the joint Cambridge Crystallographic Data Centre and Fachinformationszentrum Karlsruhe Access Structures service.

Computational details

All quantum-chemical calculations in Karlsruhe were performed with the TURBOMOLE program package.^[53] The resolution-of-the-identity (RI) approximation was used for all two-electron integrals. The equilibrium geometries were optimized at the PBE0-D3(BJ) level of theory,^[26,54] and the electronic excitations were calculated at the CD-evGW(10)/BSE level of theory (eigenvalue-only self-consistent GW (evGW)^[55] employing contour deformation (CD)^[24c] for highest 10 occupied and lowest 10 unoccupied orbitals followed by the Bethe-Salpeter equation (BSE)^[24a,b] approach). For further computational details see Supporting Information. The quantum-chemical calculations performed in Kaiserslautern were done as follows: the crystal structures were used as input structures. Geometry optimizations were performed with the Bery algorithm of Gaussian 09^[56] by using energies and gradients computed by TURBOMOLE.^[53a] All calculations were performed with the functional B3LYP with dispersion correction (no three-body interaction) (D3(BJ)).^[26,54a]

Static spectroscopy

Static UV/Vis absorption spectra were recorded on Jasco-V670 and Perkin Elmer Lambda 900 spectrophotometers. Solutions were prepared in cuvettes of 1 or 10 mm optical path length. The spectra

of solid samples were recorded on single thin transparent films on CaF_2 substrate. Decadic extinction coefficients in DCM were determined via ground state absorption spectra at given concentration and optical path length. The presented extinction coefficients are averaged over the results achieved at both instruments, error bars corresponding to the absolute deviations.

Femtosecond transient absorption in solution and solid phase

The UV/Vis fs-TA pump-probe measurements were performed based on a Ti:Sa chirped pulse regenerative amplifier system (*Coherent Libra*, 120 fs pulse duration FWHM, 4 mJ/pulse at 800 nm, 1 kHz repetition rate). The excitation pulses with 240–380 nJ per pulse at 350 nm were generated by an optical parametric amplifier (*Light Conversion TOPAS-Prime*) with focal width of $\approx 100 \mu\text{m}$ FWHM at sample position. The probe pulses (broad spectral continuum) were generated from weak pulses at 800 nm via self-phase-modulation in a moving CaF_2 window, with focal width of $\approx 40 \mu\text{m}$ at sample position. The probe pulses were spectrally dispersed and detected with an integrated 512-pixel PDA camera device (*Stresing*). For time delay (up to 1 ns) between pump and probe pulse, a delay stage (*Physik Instrumente, PI*) was used and each second pump pulse was blocked by a chopper to obtain pump-induced absorbance differences. Pump- and probe-pulse were superimposed in the sample with polarization in magic angle (54.7°) configuration. Time-zero at each probe-wavelength and system response time (260 fs) were obtained by pump-probe experiments in oxazin-4 or coumarine-152 dyes. For the solution experiments the complexes were dissolved in DCM (UVASOL grade), with an optical path length of 1 mm and optical density of 1 at the excitation wavelength (350 nm). Thin films of pure **CuL**, **CuLH** and **Cu₂L'** (not for **Cu₂L'H₂**, due to poor solubility) were obtained via spin-coating (*Ossila*, Spin Coater 3.0) from DCM-solutions with optical density of 0.35–0.47 at 350 nm and effectively doubling the OD by matching two films of each kind face-to-face. During measurements samples were rotated and moved perpendicular to the laser beam to provide fresh sample conditions. Static absorption spectra were taken before and after the fs-experiments to ensure sample integrity. All experiments were performed at room temperature. The pump-induced absorption difference data $\Delta A(t, \lambda)$ of the transient UV/VIS experiments were analyzed using the multiexponential global fit function

$$\Delta A(t, \lambda) = A_0(\lambda) + \sum_{i=1}^N A_i(\lambda) \cdot e^{-t/\tau_i} \quad (3)$$

with the decay-associated spectra (DAS) $A_i(\lambda)$, and the corresponding time constants τ_i , beginning at time delay of 200 fs.

Luminescence spectroscopy

Emission and excitation spectra in solution were recorded with a Fluoromax 4 from *Horiba Jobin*. All the solutions were air-free by letting Ar bubbling inside for 10 minutes at least. Lifetime experiments were performed by time-correlated single-photon counting method (TCSPC) with a DeltaTime kit for DeltaDiode source on FluoroMax systems, including DeltaHub and DeltaDiode controller. NanoLED 370 was used as the excitation source ($\lambda = 366 \text{ nm}$). Static temperature dependent (20–290 K at the sample) emission spectra were recorded in the solid state with a FluoroMax-2 (*Horiba Jobin-Yvon*) spectrometer using a closed cycle helium cryostat (ARS Model DE-202 A). The cryo cooler was equipped with a copper pellet holder and CaF_2 windows. KBr pellets of the four complexes were prepared by mixing (1.5 mg for **CuL** and **CuLH**; 2.2 mg for

CuL' and **CuL'H**) with dry KBr (ca. 200 mg, stored in a compartment dryer at 80°C , purchased from Merck) and grinding to a homogeneous mixture. Neat films were prepared by spraying a solution of the compound in CH_2Cl_2 on a CaF_2 substrate (13 mm diameter, 1 mm thick), followed by evaporation of the solvent. The luminescence lifetimes were determined with the time-correlated single photon counting technique (TCSPC) at temperatures of 5–290 K with an analogous cryostat (*ColdEdge*, 101 J cryocooler). Data were recorded with a DeltaFlex (*Horiba Scientific*) spectrometer. The sample was excited with short light pulses of a SpectralLED (390 nm) and the emission monochromator was set to the corresponding emission maximum ($\lambda_{\text{max}} = 500\text{--}541 \text{ nm}$). The emitted light was detected with a picosecond photon counting (PPT) detection module. In all the time-resolved luminescence experiments a long pass filter (475 nm or 500 nm) was mounted between the sample and the emission monochromator to prevent scattered excitation light from reaching the detector. Average lifetimes were calculated using the amplitude average lifetime, which is defined by

$$\tau_{av} = \sum_i a_i \tau_i \quad (4)$$

Step-scan FTIR spectroscopy

Step-scan FTIR experiments were performed with a *Bruker Vertex 80v* FTIR spectrometer, operated in the step-scan mode. Temperature dependent measurements were performed at 290 K and 20 K by the use of KBr pellets and neat films. The samples were prepared as described for the solid state luminescence spectroscopy and cooled using the cryostat ARS Model DE-202 A. A liquid-nitrogen-cooled mercury cadmium telluride (MCT) detector (*Kolmar Tech.*, Model KV100-1-B-7/190) with a rise time of 25 ns, connected to a fast preamplifier and a 14-bit transient recorder board (*Spectrum Germany*, M3I4142, 400 MS^{-1}), was used for signal detection and processing. The laser setup includes the Q-switched Nd:YAG lasers *Innolas SpitLight 1000.2* and *Innolas SpitLight Evo I* generating pulses with a band-width of 6 ns at repetition rates of 10 Hz and 100 Hz, respectively. Apart from the measurements on KBr pellets of the neutral systems **CuL** and **Cu₂L'** at 20 K (10 Hz), all the experiments were performed at 100 Hz. The third harmonic (355 nm) of the Nd:YAG laser was used for sample excitation. The UV pump beam was attenuated to 2.0 mJ and 0.2 mJ per shot at a diameter of 9 mm for measurements on KBr pellets and neat films, respectively. The beam was directed onto the sample and adjusted to have a maximal overlap with the IR beam of the spectrometer. The sample chamber was equipped with anti-reflection-coated germanium filters to prevent the entrance of laser radiation into the detector and interferometer compartments. The time delay between the start of the experiment and the UV laser pulse was controlled with a *Stanford Research Systems DG535* delay generator and the time where the laser pulse reached the sample was set as zero point in all spectra. The temporal resolution was set to 20 ns or 100 ns. The spectral region was limited by undersampling to $0\text{--}1975 \text{ cm}^{-1}$ or $988\text{--}1975 \text{ cm}^{-1}$ with a spectral resolution of 4 cm^{-1} resulting in 1110 and 555 interferogram points, respectively. An IR broad band filter ($850\text{--}1750 \text{ cm}^{-1}$) and the CaF_2 windows (no IR transmission $< 1000 \text{ cm}^{-1}$) of the cryostat prevented problems when performing a Fourier transformation (i.e. no IR intensity outside the measured region should be observed). FTIR ground state spectra were recorded systematically to check for sample degradation. A more detailed description of the step-scan setup is given elsewhere.^[46a,b,57]

Ion-trap mass spectrometry (ESI-MS)

Ion-trap mass spectrometric analyses were performed using a Paul-type 3D quadrupole ion trap mass spectrometer (*Bruker Daltonics*, amaZon speed) which was modified for laser irradiation experiments.^[35a,58] For examination of trapped ions in positive ion mode, solutions of $[\text{CuLH}]\text{BF}_4$, $[\text{Cu}_2\text{L}'\text{H}_2](\text{BF}_4)_2$ and $[\text{Cu}_2\text{L}'\text{H}_2](\text{PF}_6)_2$ in methanol ($c=10^{-6}$ M) were electrosprayed (ESI needle at 4.5 kV) at a continuous infusion rate of $120 \mu\text{l h}^{-1}$ with coaxial flow of nitrogen sheath gas (7 psi, 483 mbar) as support. Also, nitrogen was used as drying gas (4 l min^{-1} , 180°C) to assist the desolvation process. The mass-spectra were recorded in enhanced resolution scan mode (8100 amu s^{-1} , ca. 0.25 FWHM) with a mass isolation window of $\Delta m/z=9$. The instrument was controlled using the trapControl 7.4 software (*Bruker Daltonics*) and spectra were analyzed using the dataanalysis 4.4 software (*Bruker Daltonics*).

Gas phase UV-photodissociation (UV PD, τ -PD)

The experimental setup for photodissociative action spectroscopy was described elsewhere in detail.^[35b,59] Shortly, a femto- or nanosecond, respectively, UV-pump (λ_{pump} : 350–370 nm, $0.3 \mu\text{J}$) beam is focused ($f=50$ cm) and quasi-collinearly combined with a femto-second NIR-probe (λ_{probe} : 1200 nm, $130 \mu\text{J}$) beam in a Paul-type ion trap (~ 1 mm diameter) through fused silica window (3 mm thickness) of the modified mass spectrometer. For static photodissociation spectra only the pump beam (femto- or nanosecond pulses, respectively) is used and manually scanned in 3–5 nm steps in the range of 240–400 nm with a constant pulse energy ($2 \mu\text{J}$) controlled by neutral density filters and an irradiation time of 100 ms, so that each ion packet was irradiated with ~ 100 UV pulses followed by mass spectrometric analysis. The individual (Y_i) and total fragment yields (TFY) were calculated from the resulting mass spectra using

$$Y_i = F_i / (\sum F_i + P) \quad (5)$$

$$\text{TFY} = \sum F_i / (\sum F_i + P) \quad (6)$$

where F_i and P were the integrated mass peak intensities of the fragments and precursor ions and $\sum F_i$ represents the sum of all fragment product intensities. For static PD spectra the resulting fragment yields were normalized to photon number using

$$N = E_{\text{pulse}} \cdot \lambda / (h \cdot c) \quad (7)$$

For τ -PD experiments an average of 12 scans for each time window was used. A convolution of a Gaussian system response function with a multiexponential decay function in accordance with

$$S(t) = \sum_i A_i \left(\exp\left(-\frac{t}{\tau_i}\right) \times g(t, t_0, t_p) \right) \quad (8)$$

was used to fit the transient data using *Origin 2021* software (τ_i decay time constants, t_0 time zero, t_p FWHM of Gaussian, A_i amplitude of τ_i).

Femto- and nanosecond time-resolved transient photodissociation (τ -PD)

The femtosecond pump-probe experiments were performed using a Ti:Sa chirped pulse cryogenic regenerative amplifier system (*KMLabs*, Wyvern 1000TM) with an output pulse of ~ 780 nm (982 Hz, 3.1 W, FWHM ~ 50 fs). This pump beam was split in order to pump two nonlinear frequency converters (*Light Conversion*,

TOPAS-C) to generate tunable wavelength output (tuning range: 240–2600 nm). A delay stage (*Physik Instrumente*, PI) was used to generate time delay between pump and probe pulses for femto-second transient photodissociation measurements. For the ns pump/fs probe experimental setup with two pulsed laser systems, the femtosecond amplified laser output (at ca. 1 kHz) is used as the master clock and a ns kHz laser system (see below) is synchronized with electronically variable time delay between the ns pulse and the following (next) fs pulse. The femtosecond seed laser pulse is picked up by a fast photodiode (*Thorlabs*, DET10 A/M) to start a delay generator (*Stanford Research Systems*, Model DG645) which then triggers at appropriate delay a second, the main, delay generator. This configuration is used because of the necessity of a negative pump-probe delay $\Delta t < 0$ which functionality is not offered in the used delay generators.^[44] The first delay generator creates a variable pre-delay which is variably controlled by the data acquisition PC using a *LabView2018* program. The main delay generator is triggered by the first one and generates two trigger output pulses for the *EKSPLA* NT242: first a pump trigger signal and, at appropriate delay, second a Q-switch trigger signal which eventually releases the ns laser pulse. For an *in operando* check of the time overlap of the two pulses another fast photodiode (*Soliton* EOT ET-2000) at the optical output of the ion trap was used and the signal monitored on an oscilloscope (*Tektronix* DPO4101B). The resulting time delay has a time window of up to 200 μs . The time resolution is currently limited by a jitter in the regenerative amplifier switchout of the Wyvern system to ca. 50 ns, but it should be possible to reduce it to < 1 ns.

Nanosecond kHz OPO laser system

Nanosecond laser pulses were generated using a tunable diode-pumped OPO Laser System (*EKPSLA*, NT242). The 1064 nm fundamental pulse generated by a Q-switched diode-pumped Nd:YAG pump laser NL210 with a pulse duration of 4–6 ns and a repetition rate of 1 kHz was split and frequency doubled to 532 nm. Lastly, the third harmonic beam was generated to pump the nonlinear type-II BBO crystals for the OPO processes to obtain wavelengths in the range of 405–2600 nm. To achieve shorter wavelengths, a second harmonic and a sum frequency generator were used combining with the remaining fundamental Nd:YAG beam. The resulting wavelengths could be easily adjusted in the range of 210–2600 nm.

Acknowledgements

This work is supported by the DFG-funded Collaborative Research Centre (SFB) TRR 88 on Cooperative Effects in Homo- and Heterometallic Complexes “3MET” (Projects B9, C1, C2 and C4). The opportunity to use the cluster ELWE of Allianz für Hochleistungsrechnen Rheinland-Pfalz (AHRP) for calculations presented in this work is greatly acknowledged. C.R. and R.D. are thankful to the Laboratory for Advanced Spin Engineering (LASE, TUK) for laser support. We would like to appreciate the enduring and inspiring partnership in “3MET” and thank Gereon Niedner-Schatteburg (TUK) and (CB²) Stefan Bräse (KIT) for continuous support. Open Access funding enabled and organized by Projekt DEAL.

Conflict of Interest

The authors declare no conflict of interest.

Keywords: copper(I) complexes · cooperative effects · flattening distortion · photosensitizers · time-resolved spectroscopy

- [1] a) L. P. Ravaro, K. P. Zaroni, A. S. de Camargo, *Energy Reports* **2020**, *6*, 37–45; b) C. Bizzarri, E. Spuling, D. M. Knoll, D. Volz, S. Bräse, *Coord. Chem. Rev.* **2018**, *373*, 49–82; c) R. Hamze, J. L. Peltier, D. Sylvinson, M. Jung, J. Cardenas, R. Haiges, M. Soleilhavoup, R. Jazsar, P. I. Djurovich, G. Bertrand, *Science* **2019**, *363*, 601–606; d) H. Yersin, *Highly efficient OLEDs: Materials based on thermally activated delayed fluorescence*, John Wiley & Sons, **2019**.
- [2] a) C. Sandoval-Pauker, G. Molina-Aguirre, B. Pinter, *Polyhedron* **2021**, *115105*; b) A. Hossain, A. Bhattacharyya, O. Reiser, *Science* **2019**, *364*; c) J. Kim, D. R. Whang, S. Y. Park, *ChemSusChem* **2017**, *10*, 1883–1886.
- [3] a) K. E. Dalle, J. Warnan, J. J. Leung, B. Reuillard, I. S. Karmel, E. Reisner, *Chem. Rev.* **2019**, *119*, 2752–2875; b) A. Rosas-Hernández, C. Steinlechner, H. Junge, M. Beller, *Green Chem.* **2017**, *19*, 2356–2360; c) H. Takeda, H. Kamiyama, K. Okamoto, M. Irimajiri, T. Mizutani, K. Koike, A. Sekine, O. Ishitani, *J. Am. Chem. Soc.* **2018**, *140*, 17241–17254; d) H. Takeda, K. Ohashi, A. Sekine, O. Ishitani, *J. Am. Chem. Soc.* **2016**, *138*, 4354–4357; e) W. J. Ong, L. K. Putri, A. R. Mohamed, *Chemistry—A European Journal* **2020**, *26*, 9710–9748; f) H. Rao, J. Bonin, M. Robert, *ChemSusChem* **2017**, *10*, 4447–4450; g) Y. Sakaguchi, A. Call, M. Cibian, K. Yamauchi, K. Sakai, *Chem. Commun.* **2019**, *55*, 8552–8555; h) L. L. Gracia, L. Luci, C. Bruschi, L. Sambri, P. Weis, O. Fuhr, C. Bizzarri, *Chemistry (Weinheim an der Bergstrasse, Germany)* **2020**, *26*, 9929; i) J. Schneider, H. Jia, J. T. Muckerman, E. Fujita, *Chem. Soc. Rev.* **2012**, *41*, 2036–2051.
- [4] a) N. Armadori, G. Accorsi, F. Cardinali, A. Listorti, *Photochemistry and Photophysics of Coordination Compounds I* **2007**, 69–115; b) A. C. Hernandez-Perez, S. K. Collins, *Acc. Chem. Res.* **2016**, *49*, 1557–1565; c) M. Wallesch, D. Volz, D. M. Zink, U. Schepers, M. Nieger, T. Baumann, S. Bräse, *Chemistry—A European Journal* **2014**, *20*, 6578–6590.
- [5] Y. Zhang, M. Schulz, M. Waechtler, M. Karnahl, B. Dietzek, *Coord. Chem. Rev.* **2018**, *356*, 127–146.
- [6] a) Y. Zhang, L. Zedler, M. Karnahl, B. Dietzek, *Phys. Chem. Chem. Phys.* **2019**, *21*, 10716–10725; b) Y. Zhang, P. Traber, L. Zedler, S. Kupfer, S. Gräfe, M. Schulz, W. Frey, M. Karnahl, B. Dietzek, *Phys. Chem. Chem. Phys.* **2018**, *20*, 24843–24857.
- [7] A. Kaeser, M. Mohankumar, J. Mohanraj, F. Monti, M. Holler, J.-J. Cid, O. Moudam, I. Nierengarten, L. Karmazin-Brelot, C. Duhayon, *Inorg. Chem.* **2013**, *52*, 12140–12151.
- [8] a) L. Bergmann, G. J. Hedley, T. Baumann, S. Bräse, I. D. Samuel, *Sci. Adv.* **2016**, *2*, e1500889; b) M. Grupe, F. Böppler, M. Theiß, J. M. Busch, F. Dietrich, D. Volz, M. Gerhards, S. Bräse, R. Diller, *Phys. Chem. Chem. Phys.* **2020**, *22*, 14187–14200; c) C. Bizzarri, C. Fléchon, O. Fenwick, F. Cacialli, F. Polo, M. D. Gálvez-López, C.-H. Yang, S. Scintilla, Y. Sun, R. Fröhlich, *ECS Journal of Solid State Science and Technology* **2016**, *5*, R83; d) J.-L. Chen, X.-F. Cao, J.-Y. Wang, L.-H. He, Z.-Y. Liu, H.-R. Wen, Z.-N. Chen, *Inorg. Chem.* **2013**, *52*, 9727–9740; e) F. Ferrari, J. Braun, C. E. Anson, B. D. Wilts, D. Moatsou, C. Bizzarri, *Molecules* **2021**, *26*, 2567; f) Q. Zhang, X.-L. Chen, J. Chen, X.-Y. Wu, R. Yu, C.-Z. Lu, *Dalton Trans.* **2015**, *44*, 10022–10029; g) L. Lin, D.-H. Chen, R. Yu, X.-L. Chen, W.-J. Zhu, D. Liang, J.-F. Chang, Q. Zhang, C.-Z. Lu, *J. Mater. Chem. C* **2017**, *5*, 4495–4504.
- [9] C. Bruschi, X. Gui, N. Salaeh-arae, T. Barchi, O. Fuhr, S. Lebedkin, W. Klopfer, C. Bizzarri, *Eur. J. Inorg. Chem.* doi.org/10.1002/ejic.202100653.
- [10] a) P. A. F. Cortés, M. Marx, M. Trose, M. Beller, *Chem Catalysis* **2021**; b) G. Noirbent, F. Dumur, *Catalysts* **2020**, *10*, 953; c) Y. Yamazaki, T. Onoda, J. Ishikawa, S. Furukawa, C. Tanaka, T. Utsugi, T. Tsubomura, *Front. Chem.* **2019**, *7*, 288.
- [11] a) G. B. Shaw, C. D. Grant, H. Shirota, E. W. Castner, G. J. Meyer, L. X. Chen, *J. Am. Chem. Soc.* **2007**, *129*, 2147–2160; b) M. Iwamura, S. Takeuchi, T. Tahara, *Acc. Chem. Res.* **2015**, *48*, 782–791.
- [12] a) H. Yersin, R. Czerwieńiec, M. Z. Shafikov, A. F. Suleymanova, *ChemPhysChem* **2017**, *18*, 3508–3535; b) S. Garakyaraghi, C. E. McCusker, S. Khan, P. Koutnik, A. T. Bui, F. N. Castellano, *Inorg. Chem.* **2018**, *57*, 2296–2307; c) P. A. Papanikolaou, N. V. Tkachenko, *Phys. Chem. Chem. Phys.* **2013**, *15*, 13128–13136.
- [13] A. Stoianov, C. Gourlaouen, S. Vela, C. Daniel, *J. Phys. Chem. A* **2018**, *122*, 1413–1421.
- [14] C. Bizzarri, A. P. Arndt, S. Kohaut, K. Fink, M. Nieger, *J. Organomet. Chem.* **2018**, *871*, 140–149.
- [15] a) G. Niedner-Schatteburg, *Clusters—Contemporary Insight in Structure and Bonding* **2016**, 1–40; b) G. Niedner-Schatteburg, in *Clusters—Contemporary Insight in Structure and Bonding*, Springer, **2017**, pp. 375–376.
- [16] a) M. J. Leidl, F.-R. Kühle, H. A. Mayer, L. Wesemann, H. Yersin, *J. Phys. Chem. A* **2013**, *117*, 11823–11836; b) R. Czerwieńiec, M. J. Leidl, H. H. Homeier, H. Yersin, *Coord. Chem. Rev.* **2016**, *325*, 2–28.
- [17] P. A. Scattergood, P. I. Elliott, *Dalton Trans.* **2017**, *46*, 16343–16356.
- [18] J. I. Mapley, D. A. Ross, C. J. McAdam, K. C. Gordon, J. D. Crowley, *J. Coord. Chem.* **2019**, *72*, 1378–1394.
- [19] G. Gritzner, J. Kuta, *Pure Appl. Chem.* **1984**, *56*, 461–466.
- [20] a) E. Kimura, X. Bu, M. Shionoya, S. Wada, S. Maruyama, *Inorg. Chem.* **1992**, *31*, 4542–4546; b) E. Kimura, S. Wada, M. Shionoya, Y. Okazaki, *Inorg. Chem.* **1994**, *33*, 770–778; c) C. A. Craig, L. O. Spreer, J. W. Otvos, M. Calvin, *J. Phys. Chem.* **1990**, *94*, 7957–7960; d) J. L. Grant, K. Goswami, L. O. Spreer, J. W. Otvos, M. Calvin, *J. Chem. Soc. Dalton Trans.* **1987**, 2105–2109; e) C. Herrero, A. Quaranta, S. El Ghachtouli, B. Vauzeilles, W. Leibl, A. Aukauloo, *Phys. Chem. Chem. Phys.* **2014**, *16*, 12067–12072; f) M. F. Kuehnel, C. D. Sahn, G. Neri, J. R. Lee, K. L. Orchard, A. J. Cowan, E. Reisner, *Chem. Sci.* **2018**, *9*, 2501–2509; g) M. A. Méndez, P. Voyage, H. H. Girault, *Angew. Chem.* **2011**, *123*, 7529–7532; *Angew. Chem. Int. Ed.* **2011**, *50*, 7391–7394; h) K. Mochizuki, S. Manaka, I. Takeda, T. Kondo, *Inorg. Chem.* **1996**, *35*, 5132–5136; i) C. R. Schneider, H. S. Shafaat, *Chem. Commun.* **2016**, *52*, 9889–9892.
- [21] a) M. Iwamura, H. Watanabe, K. Ishii, S. Takeuchi, T. Tahara, *J. Am. Chem. Soc.* **2011**, *133*, 7728–7736; b) M. W. Mara, N. E. Jackson, J. Huang, A. B. Stickrath, X. Zhang, N. A. Gothard, M. A. Ratner, L. X. Chen, *J. Phys. Chem. B* **2013**, *117*, 1921–1931; c) M. T. Miller, P. K. Gantzel, T. B. Karpishin, *J. Am. Chem. Soc.* **1999**, *121*, 4292–4293.
- [22] a) A. D. Becke, *J. Chem. Phys.* **1993**, *98*, 1372–1377; b) P. J. Stephens, F. J. Devlin, C. F. Chabalowski, M. J. Frisch, *J. Phys. Chem.* **1994**, *98*, 11623–11627.
- [23] J. P. Perdew, M. Ernzerhof, K. Burke, *J. Chem. Phys.* **1996**, *105*, 9982–9985.
- [24] a) K. Krause, W. Klopfer, Wiley Online Library, **2017**; b) X. Gui, C. Holzer, W. Klopfer, *J. Chem. Theory Comput.* **2018**, *14*, 2127–2136; c) C. Holzer, W. Klopfer, *J. Chem. Phys.* **2019**, *150*, 204116.
- [25] A. Dreuw, M. Head-Gordon, *J. Am. Chem. Soc.* **2004**, *126*, 4007–4016.
- [26] S. Grimme, J. Antony, S. Ehrlich, H. Krieg, *J. Chem. Phys.* **2010**, *132*, 154104.
- [27] B. Goswami, T. J. Feuerstein, R. Yadav, S. Lebedkin, P. J. Boden, S. T. Steiger, G. Niedner-Schatteburg, M. Gerhards, M. M. Kappes, P. W. Roesky, *Chemistry—A European Journal* **2021**.
- [28] a) S. V. Kruppa, C. Groß, X. Gui, F. Böppler, B. Kwasigroch, Y. Sun, R. Diller, W. Klopfer, G. Niedner-Schatteburg, C. Riehn, *Chemistry—A European Journal* **2019**, *25*, 11176–11176; b) N. C. Polfer, P. Dugourd, *Laser photodissociation and spectroscopy of mass-separated biomolecular ions*, Springer, **2013**; c) J. S. Brodbelt, *Chem. Soc. Rev.* **2014**, *43*, 2757–2783.
- [29] C. L. Linfoot, M. J. Leidl, P. Richardson, A. F. Rausch, O. Chepelin, F. J. White, H. Yersin, N. Robertson, *Inorg. Chem.* **2014**, *53*, 10854–10861.
- [30] a) H. Yersin, A. F. Rausch, R. Czerwieńiec, T. Hofbeck, T. Fischer, *Coord. Chem. Rev.* **2011**, *255*, 2622–2652; b) R. Czerwieńiec, K. Kowalski, H. Yersin, *Dalton Trans.* **2013**, *42*, 9826–9830.
- [31] N. Lüdtkke, J. Föllner, C. M. Marian, *Phys. Chem. Chem. Phys.* **2020**, *22*, 23530–23544.
- [32] G. Capano, M. Chergui, U. Rothlisberger, I. Tavernelli, T. J. Penfold, *J. Phys. Chem. A* **2014**, *118*, 9861–9869.
- [33] C. Müller, M. Schulz, M. Obst, L. Zedler, S. Gräfe, S. Kupfer, B. Dietzek, *J. Phys. Chem. A* **2020**, *124*, 6607–6616.
- [34] C. Ma, C. T.-L. Chan, W.-M. Kwok, C.-M. Che, *Chem. Sci.* **2012**, *3*, 1883–1892.
- [35] a) D. Imanbaev, Y. Nosenko, C. Kerner, K. Chevalier, F. Rupp, C. Riehn, W. Thiel, R. Diller, *Chem. Phys.* **2014**, *442*, 53–61; b) D. Imanbaev, J. Lang, M. F. Gelin, S. Kaufhold, M. G. Pfeffer, S. Rau, C. Riehn, *Angew. Chem.* **2017**, *129*, 5563–5566; *Angew. Chem. Int. Ed.* **2017**, *56*, 5471–5474.
- [36] a) D. Nolting, T. Schultz, I. Hertel, R. Weinkauff, *Phys. Chem. Chem. Phys.* **2006**, *8*, 5247–5254; b) H. Kang, C. Jouvét, C. Dedonder-Lardeux, S. Martrenchard, C. Charrière, G. Gregoire, C. Desfrancois, J. Schermann, M. Barat, J. Fayette, *J. Chem. Phys.* **2005**, *122*, 084307; c) G. Grégoire, B.

- Lucas, M. Barat, J. Fayeton, C. Dedonder-Lardeux, C. Juvet, *The European Physical Journal D* **2009**, *51*, 109–116.
- [37] T. Katayama, T. Northey, W. Gawelda, C. J. Milne, G. Vankó, F. A. Lima, Z. Németh, S. Nozawa, T. Sato, D. Khakhulin, *Nat. Commun.* **2019**, *10*, 1–8.
- [38] a) R. Monni, G. Capano, G. Auböck, H. B. Gray, A. Vlček, I. Tavernelli, M. Chergui, *Proc. Natl. Acad. Sci. USA* **2018**, *115*, E6396–E6403; b) M.-O. Winghart, J.-P. Yang, M. Vonderach, A.-N. Unterreiner, D.-L. Huang, L.-S. Wang, S. Kruppa, C. Riehn, M. M. Kappes, *J. Chem. Phys.* **2016**, *144*, 054305.
- [39] a) C. Mueck-Lichtenfeld, S. Grimme, *Dalton Trans.* **2012**, *41*, 9111–9118; b) T. Wall, M. Leist, F. Dietrich, W. R. Thiel, M. Gerhards, *ChemPlusChem* **2021**, *86*, 622–628.
- [40] Y. Sun, V. Lemaur, J. I. Beltran, J. Cornil, J. Huang, J. Zhu, Y. Wang, R. Fröhlich, H. Wang, L. Jiang, *Inorg. Chem.* **2016**, *55*, 5845–5852.
- [41] R. Czerwieniec, J. Yu, H. Yersin, *Inorg. Chem.* **2011**, *50*, 8293–8301.
- [42] R. Czerwieniec, H. Yersin, *Inorg. Chem.* **2015**, *54*, 4322–4327.
- [43] a) M. Mohankumar, M. Holler, E. Meichsner, J.-F. o. Nierengarten, F. D. R. Niess, J.-P. Sauvage, B. A. Delavaux-Nicot, E. Leoni, F. Monti, J. M. Malicka, *J. Am. Chem. Soc.* **2018**, *140*, 2336–2347; b) D. Felder, J.-F. Nierengarten, F. Barigelletti, B. Ventura, N. Armaroli, *J. Am. Chem. Soc.* **2001**, *123*, 6291–6299; c) A. J. Lees, *Comments Inorg. Chem.* **1995**, *17*, 319–346.
- [44] E. Riedle, M. Wenniger, Chapter 16 in: B. König, *Chemical photocatalysis*, Walter de Gruyter GmbH & Company KG, **2013**.
- [45] a) J. R. Schoonover, G. F. Strouse, *Chem. Rev.* **1998**, *98*, 1335–1356; b) G. D. Smith, M. S. Hutson, Y. Lu, M. T. Tierney, M. W. Grinstaff, R. A. Palmer, *Appl. Spectrosc.* **2001**, *55*, 637–642; c) J. Torres-Alacan, P. Vöhringer, *Chemistry—A European Journal* **2017**, *23*, 6746–6751; d) P. Boden, P. Di Martino-Fumo, G. Niedner-Schatteburg, W. W. Seidel, K. Heinze, M. Gerhards, *Phys. Chem. Chem. Phys.* **2021**.
- [46] a) F. Böppler, M. Zimmer, F. Dietrich, M. Grupe, M. Wallesch, D. Volz, S. Bräse, M. Gerhards, R. Diller, *Phys. Chem. Chem. Phys.* **2017**, *19*, 29438–29448; b) M. Zimmer, F. Dietrich, D. Volz, S. Bräse, M. Gerhards, *ChemPhysChem* **2017**, *18*, 3023–3029; c) P. Boden, P. Di Martino-Fumo, J. M. Busch, F. R. Rehak, S. Steiger, O. Fuhr, M. Nieger, D. Volz, W. Klopper, S. Bräse, *Chemistry (Weinheim an der Bergstrasse, Germany)* **2021**, *27*, 5439.
- [47] S. Tschierlei, M. Karnahl, N. Rockstroh, H. Junge, M. Beller, S. Lochbrunner, *ChemPhysChem* **2014**, *15*, 3709–3713.
- [48] G. Li, R. S. Nobuyasu, B. Zhang, Y. Geng, B. Yao, Z. Xie, D. Zhu, G. Shan, W. Che, L. Yan, *Eur. J. Chem.* **2017**, *23*, 11761.
- [49] B. Dereka, A. Rosspeintner, Z. Li, R. Liska, E. Vauthey, *J. Am. Chem. Soc.* **2016**, *138*, 4643–4649.
- [50] a) C. Förster, K. Heinze, *Chem. Soc. Rev.* **2020**, *49*, 1057–1070; b) O. S. Wenger, *J. Am. Chem. Soc.* **2018**, *140*, 13522–13533.
- [51] G. M. Sheldrick, *Acta Crystallographica Section A: Foundations and Advances* **2015**, *71*, 3–8.
- [52] G. M. Sheldrick, *Acta Crystallographica Section C: Structural Chemistry* **2015**, *71*, 3–8.
- [53] a) F. Furche, R. Ahlrichs, C. Hättig, W. Klopper, M. Sierka, F. Weigend, *WIREs Comput. Mol. Sci.* **2014**, *4*, 91–100; b) TURBOMOLE V7.4, 2019, a development of University of Karlsruhe and Forschungszentrum Karlsruhe GmbH, 1989–2007, TURBOMOLE GmbH, since 2007; available from <http://www.turbomole.com>.
- [54] a) S. Grimme, S. Ehrlich, L. Goerigk, *Journal of computational chemistry* **2011**, *32*, 1456–1465; b) J. P. Perdew, K. Burke, M. Ernzerhof, *Rev. Lett* **1997**, *78*, 1396; c) J. P. Perdew, K. Burke, M. Ernzerhof, *Physical review letters* **1996**, *77*, 3865.
- [55] X. Blase, C. Attaccalite, V. Olevano, *Physical Review B* **2011**, *83*, 115103.
- [56] M. Frisch, G. Trucks, H. Schlegel, G. Scuseria, M. Robb, J. Cheeseman, G. Scalmani, V. Barone, G. Petersson, H. Nakatsuji et al., *Gaussian, Inc., Wallingford CT* **2016**.
- [57] M. Zimmer, F. Rupp, P. Singer, F. Walz, F. Breher, W. Klopper, R. Diller, M. Gerhards, *Physical Chemistry Chemical Physics* **2015**, *17*, 14138–14144.
- [58] a) Y. Nosenko, F. Menges, C. Riehn, G. Niedner-Schatteburg, *Physical Chemistry Chemical Physics* **2013**, *15*, 8171–8178; b) S. Kruppa, F. Böppler, Y. Nosenko, S. Walg, R. Diller, C. Riehn, in *International Conference on Ultrafast Phenomena*, Optical Society of America, **2016**, p. UW4 A. 33; c) J. Martens, G. Berden, C. R. Gebhardt, J. Oomens, *Review of Scientific Instruments* **2016**, *87*, 103108.
- [59] a) Y. Nosenko, C. Riehn, W. Klopper, *Chemical Physics Letters* **2016**, *659*, 55–60; b) S. V. Kruppa, Y. Nosenko, M.-O. Winghart, S. P. Walg, M. M. Kappes, C. Riehn, *International Journal of Mass Spectrometry* **2016**, *395*, 7–19.

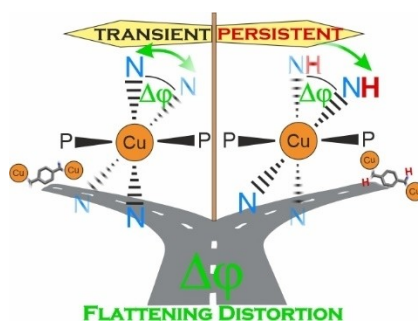
Manuscript received: July 29, 2021

Accepted manuscript online: September 22, 2021

Version of record online: ■■■, ■■■■

FULL PAPER

The comprehensive results on two mononuclear pyridyl-triazole/DPEPhos based Cu(I) complexes and its extension to their two dinuclear analogues paves the road to addressing the complex coupling of the respective monomeric units, involving various physical and chemical properties as charge, (electronic) structure and (long-lived) excited state properties, relevant for applications.



Dr. M. Grupe, P. Boden, P. Di Martino-Fumo, Dr. X. Gui, C. Bruschi, R. Israil, M. Schmitt, Dr. M. Nieger, Prof. Dr. M. Gerhards, Prof. Dr. W. Klopper, Dr. C. Riehn, Dr. C. Bizzarri, Prof. Dr. R. Diller**

1 – 21

Time-Resolved Spectroscopy and Electronic Structure of Mono- and Dinuclear Pyridyl-Triazole/DPEPhos-Based Cu(I) Complexes

